UNIVERSITY of CALIFORNIA
Santa Barbara

Aluminum Gallium Nitride / Gallium Nitride Heterojunction Bipolar Transistors

A dissertation submitted in partial satisfaction of the
requirements for the degree of

Doctor of Philosophy

in

Electrical Engineering

by

Lee S. McCarthy

Committee in charge:

Professor Umesh K. Mishra, Chair
Professor Steven DenBaars
Professor Mark Rodwell
Professor Evelyn Hu

December 2001

The dissertation of Lee S. McCarthy is approved:

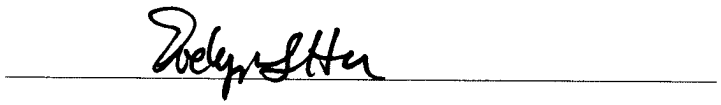

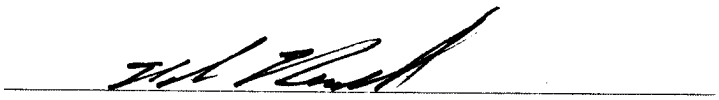

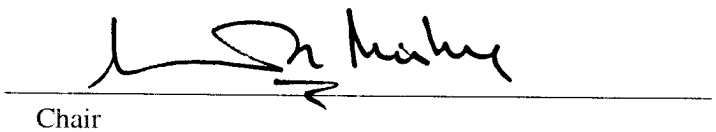

Chair

December 2001

Aluminum Gallium Nitride / Gallium Nitride Heterojunction Bipolar Transistors

by

Lee S. McCarthy

Curriculum Vitæ

Lee S. McCarthy

EDUCATION

Bachelor of Science in Electrical and Computer Engineering, University of California, Santa Barbara, June 1996
Master of Science in Electrical and Computer Engineering, University of California, Santa Barbara, June, 2000
Doctor of Philosophy in Electrical Engineering, University of California, Santa Barbara, December 2001 (expected)

PROFESSIONAL EMPLOYMENT

1996-2000 Research assistant, Department of Electrical and Computer Engineering, University of California, Santa Barbara
Sept 2000 - Sept 2001, Principal engineer for device fabrication, Nitronex Inc. Raleigh, NC.

PUBLICATIONS

L. McCarthy, P. Kozodoy, M. Rodwell, S. Denbaars, and U. Mishra. A first look at AlGaN/GaN HBTs. *Compound Semiconductor*, 4(8):16–18, 1998.

L. S. McCarthy, P. Kozodoy, M. Rodwell, S. DenBaars, and U. K. Mishra. First demonstration of an AlGaN/GaN heterojunction bipolar transistor. pages 279–84, 1999. Compound Semiconductors 1998. Proceedings of the Twenty-Fifth International Symposium on Compound Semiconductors.

L. S. McCarthy, P. Kozodoy, M. J. W. Rodwell, S. P. DenBaars, and U. K. Mishra. AlGaN/GaN heterojunction bipolar transistor. *IEEE Electron Device Letters*, 20(6) : 277–9, 1999.

L. McCarthy, Y. Smorchkova, P. Fini, H. Xing, M. Rodwell, J. Speck, S. DenBaars, and U. Mishra. HBT on leo GaN. pages 85–6, 2000. 58th DRC. Device Research Conference.

L. McCarthy, I. Smorchkova, H. Xing, P. Fini, S. Keller, J. Speck, S. P. DenBaars, M. J. W. Rodwell, and U. K. Mishra. Effect of threading dislocations on AlGaN/GaN heterojunction bipolar transistors. *Applied Physics Letters*, 78(15):2235–7, 2001.

L. S. McCarthy, I. P. Smorchkova, Xing Huili, P. Kozodoy, P. Fini, J. Limb, D. L. Pulfrey, J. S. Speck, M. J. W. Rodwell, S. P. DenBaars, and U. K. Mishra. GaN HBT: toward an rf device. *IEEE Transactions on Electron Devices*, 48(3):543–51, 2001.

J. B. Limb, L. McCarthy, P. Kozodoy, H. Xing, J. Ibbetson, Y. Smorchkova, S. P. DenBaars, and U. K. Mishra. AlGaN/GaN HBTs using regrown emitter. *Electronics Letters*, 35(19):1671–3, 1999.

J. B. Limb, H. Xing, B. Moran, L. McCarthy, S. P. DenBaars, and U. K. Mishra. High voltage operation (¿80 v) of GaN bipolar junction transistors with low leakage. *Applied Physics Letters*, 76(17):2457–9, 2000.

U. K. Mishra, R. Ventury, L. McCarthy, Y. Smorchkova, S. Keller, H. Xing,
N. Zhang, J. S. Speck, R. York, S. DenBaars, Y. F. Wu, P. Parikh, and P. Chavarkar. AlGaN-GaN HEMTs and HBTs for microwave power. pages 35–6, 2000. 58th DRC. Device Research Conference.

H. Xing, S. Keller, Y. F. Wu, L. McCarthy, I. P. Smorchkova, D. Buttari, R. Coffie, D. S. Green, G. Parish, S. Heikman, L. Shen, N. Zhang, J. J. Xu, B. P. Keller, S. P. DenBaars, and U. K. Mishra. Gallium nitride based transistors. *Journal of Physics: Condensed Matter*, 13(32):7139–57, 2001.

H. Xing, L. McCarthy, S. Keller, S. P. DenBaars, and U. K. Mishra. High current gain GaN bipolar junction transistors with regrown emitters. pages 365–9, 2000. 2000 IEEE International Symposium on Compound Semiconductors. Proceedings of the IEEE Twenty-Seventh International Symposium on Compound Semiconductors.

Abstract

Aluminum Gallium Nitride / Gallium Nitride Heterojunction Bipolar Transistors

by

Lee S. McCarthy

In the last five years, the commercial outlook for GaN optoelectronic and electronic devices has grown considerably. This dissertation is focused on efforts to develop growth and fabrication technology for the GaN HBT. The development of the HBT is motivated by a demand for high power, high frequency electronics. From the demonstration of the first AlGaN/GaN HBT in 1998, and the first HBT on LEO substrates, to the first small signal rf measurements of a GaN HBT in 2000, progress has been made in identifying the major issues in the DC and RF performance of the AlGaN/GaN HBT. Devices have been fabricated on MOCVD and MBE active layers of varying structure including compositionally graded bases, and base layers of varying thickness and doping concentration. The cause of the parasitic offset voltage in the common emitter output characteristics has been investigated, and addressed in the extrinsic regrown base HBT as well as in process improvements associated with the emitter mesa etch and the base metalization process. The effects of dislocations were investigated by fabricating devices on LEO substrates and measuring the collector-emitter leakage as a function of dislocation density and base doping profile. Finally, a process was developed for fabricating CPW compatible devices, and devices were tested and shown to have an current gain cut-off frequency of 2GHz. The gain/frequency characteristic was un-ideal, however, and finite element simulations confirm that this may be due to the low conductivity in the base.

Contents

List of Figures

List of Tables

Acknowledgements

WORKING at UC Santa Barbara, although challenging, has been a deeply rewarding experience. Beginning my undergraduate work here in 1991, then my graduate work in 1996, I have been fortunate to work with many fine researchers and benefit from the tuition of several exceptional lecturers. In particular, my advisor, Umesh Mishra has been a constant source of enthusiasm, and provided valuable technical and professional guidance over the years. This enthusiasm was first evident to me in his lectures on introductory device physics in 1993, and eventually brought me to his research group in 1996. The solid state and electronic materials research community at UCSB is a cohesive and cooperative group of exceptional depth and a world leader in its chosen fields. I have been particularly fortunate to be a member of this group. In addition to my advisor, the other members of my doctoral committee have been helpful in many aspects of the research for this dissertation. Prof. Mark Rodwell was particularly helpful in understanding aspects of the small signal performance of the devices. Prof. Evelyn Hu has been a valuable resource in understanding processing issues for the devices, and Prof. Steve DenBaars has been an asset in the area of MOCVD material growth.
Fellow researchers are perhaps the greatest resource to students, and I would particularly like to thank Dr. Primit Parikh and Dr. Yifeng Wu for their training in the art of semiconductor processing as well as much guidance over the years in my research efforts. The work of Dr. Peter Kozodoy was a vital part of the research for this dissertation. Without his constant dedication and conference in the area of MOCVD growth and device and process design, this work would not have been possible. Later, work was conducted on MBE grown material, and the effort invested by Dr. Yulia Smorchkova was likewise essential. Dr. Stacia Keller was instrumental for structures grown by MOCVD, and I would also like to thank Paul Fini, Brendan Moran, Hughues Marchand, Huili Xing, Jae Limb, Dan Green, and Andreas Stonas for their direct involvement. I would like to acknowledge some of the many graduate students in Profs. Mishra and York groups who were a constant source of advice and friendship over the years, Particularly Ramakrishna Vetury and James Champlain. Also, thanks to Amit, Nick, Jeff Yen, Rob Underwood, Prashant, Naiquian, Likun, Rob C., Paolo, Dario, Can, DJ, Sten, Amber and Elaine. Work in Prof. Mishra's group would not be possible without the support of Cathy and Lee. Jack Whaley and Bob Hill are vital in the support of the cleanroom, and thanks also to Brian in MOCVD and Valerie de Veyra in the ECE graduate student office.

I am especially grateful for those who demonstrated extraordinary faith in my abilities and made it possible for me to be here. In particular, I would like to thank Prof. Forrest Brewer and Dr. Primit Parikh as well as Prof. Mishra.

Finally, I would like to acknowledge the support of friends and family outside the department. I am grateful for their support and understanding. Thanks to Kacey, Rachel, Melinda, Louise, Jeanette, Darcy, Gianna, Aubrei, Carmella, Doug. And of course, thanks to my father and mother for their bottomless support.

1 Introduction

IN the last five years, the commercial outlook for Gallium Nitride (GaN) and its family of material alloys has grown considerably. In a decade which has witnessed many of the 'firsts' in the development of GaN, the recent progress has been intensive. With the commercialization of GaN for LEDs and the immanent release of GaN based laser diodes for the next generation of optical data storage electronics, GaN will continue to play an important role in visible wavelength optoelectronics. Arguably not far behind are a host of electronic devices that take advantage of the high critical breakdown fields associated with the large bandgap of GaN, and benefit from its high saturated electron velocities. These devices are intended to fill the strong demand for high power, high frequency electronic components. Commercial applications range from high voltage power switching to communications and beyond. Although GaN electronics products were not readily available at the time of this publication, several companies are pursuing this goal both for commercial and military applications.

The subject of this dissertation, GaN heterojunction bipolar transistors
(HBTs), follows extensive work by other researchers in the development of GaN material growth and understanding as well as processing and device design efforts. By incorporating a p-type layer, the HBT brings together the understanding of magnesium doped GaN, typically connected with opto-electronic devices with the electronic device design and processing techniques associated with GaN FETs and AlGaAs/GaAs HBTs. As the first effort at UCSB to fabricate a GaN HBT, the goal of this research was to extend the current state-of-the-art in GaN electronic devices by establishing a platform of processing, growth, and design understanding focused on the fabrication of GaN HBTs. The metric for success was the measured electronic performance of the transistors. A beneficial by-product has been the inevitable cross-over of technologies and understanding developed initially for the GaN HBTs into the more established areas of GaN optoelectronic and field effect devices.

1.1 Motivation for the development of AlGaN/GaN HBTs

The development of the AlGaN/GaN HBT is motivated by the demand for high power, high frequency electronics. Its prospects are founded in the fundamental physical properties of the material and encouraged by the success of other GaN devices. GaN is desirable for electronics applications due to projected saturated electron velocities of 2×10^7 cm/s[1], and a 3.4 eV bandgap that leads to a critical breakdown field of 2 MV/cm[2], as well as stability at high temperatures. In other III-V material systems, HBTs offer several important advantages over FETs. HBTs generally have better threshold uniformity and device linearity, as well as lower phase noise than FETs. In addition, the HBT structure inherently offers a higher ratio of output current to parasitic capacitance. The fundamental material properties described in Table 1.1 can be used in comparison with a mature material system to predict potential RF performance of these devices. Lee et al. demonstrated AlInAs/GaInAs HBTs using a transferred substrate Schottky collector technology with a power gain cutoff frequency, f_{max}, of 820 GHz [3]. If this technology were applied to a GaN bipolar structure with a 50 nm base, having a base carrier concentration of 5×10^{19} cm^{-3}, and a 100 nm thick collector, the predicted f_{max} is 200 GHz with a current gain cutoff frequency, f_t, of 200 GHz, and a 15V breakdown voltage. For power switching applications, material properties suggest that a 1 kV device with a collector thickness of 7μm, and a base thickness of 200 nm would have an f_t of 6 GHz and an f_{max} over 300 GHz. In 1991, Gao et al. used a figure of merit comparison to predict the prospects of HBTs in various material systems[4]. Table 1.2 shows a sampling of their results, suggesting the relative advantages of an AlGaN/GaN HBT. At the time, Gao had less information than is presently available regarding the characteristics of the p-type (Mg doped) base layer, and so the same base-layer figure of merit calculated for p-type Si was used for the GaN device. The bottom line of Table 1.2 was calculated using Gao's definitions:[1]

Property	*GaN*	*GaInP*	*Si*
v_{sat} [cm/s]	20×10^6	10×10^6	6×10^6
E_{crit} [MV/cm]	2	0.6	0.3

Table 1.1: Comparison of material properties relevant to RF performance

$$B_{fm} = \left(\frac{\mu_{nB}^{1/2} \mu_{pB} N_B}{\epsilon \epsilon_0} \right)^{1/2} \tag{1.1.1}$$

$$C_{fm} = v_d^{5/4} W_c^{5/4} E_c N_c \tag{1.1.2}$$

[1] $\mu_{nB}, \mu_{pB}, N_B, v_d, W_c, E_c$ represent the carrier mobilities in the base, the number of free majority carriers in the base, the electron drift velocity in the collector, the collector width, and the emitter critical breakdown field respectively.

Material System	B_{fm}	C_{fm}	$\prod_{(Al)GaAs}$
poly-Si/Si/Si	8.5×10^{16}	3.8×10^{25}	.58
AlGaAs/GaAs/AlGaAs	13.4	6.5	1.0
InP/InGaAs/InP	17.8	5.4	1.71
6H-SiC/3C-SiC/6H-SiC	8.5	37.3	5.65
AlGaN/GaN†/GaN	8.5	123.2	18.67
AlGaN/GaN‡/GaN	0.79	123.2	1.73

Table 1.2: Comparison of HBT figure of merit for HBTs in various material systems [4].
†Assumes base properties similar to Si.
‡Calculated using base material properties as reported by [5] and [6]. The third column represents the product of the figures of merit normalized to an AlGaAs/GaAs/AlGaAs DHBT.

to reflect the figure of merit using current values for majority carrier mobility and concentration, and a more reasonable estimation for the minority carrier mobility. The disparity in the two results illustrates that the realization of the potential for GaN HBTs is not trivial, and may face fundamental problems. The focus of this dissertation is on the identification and understanding of those issues.

1.2 Research background

In context, research into electronic devices in the III-N material systems is relatively immature. Figure 1.1 shows the number of INSPEC[2] citations for conventional HBTs, GaN based FETs, and AlGaN/GaN HBTs. Much of the early work on AlGaAs/GaAs HBTs was limited by the difficulty in achieving high quality heterojunctions with liquid phase epitaxy (LPE). In 1981, devices grown by MBE began to appear, leading to improved performance. In AlGaAs/GaAs HBTs, beryllium dopant diffusion and therefore junction placement remained a problem until the introduction of carbon doping, which begins to appear in the literature around 1988. More recently, the focus has shifted toward scaling of these devices. The amount of publications addressing these issues reflects the substantial effort required in conventional III-V HBTs to approach the theoretical potential of the material system. In comparison, to date little has been published in the literature regarding AlGaN/ GaN HBTs, and the research background in the field is scarce. The majority of electronic device research in GaN focuses on field effect transistors (FETs), specifically the heterojunction field effect transistor or high electron mobility transistor (HEMT). In 1993, the first FET was reported by Khan et al.[7]. Several reports followed with the first microwave measurements of GaN FETs reported by Binari et al.[8] with an f_t and f_{max} of 8 GHz and 18 GHz respectively. Next, in 1996, the first power measurements were made on GaN HEMTs by Wu et al.[9], with a report of 1.1 W/mm at 2 GHz. Quickly, reported output powers increased with recent reports as high as 9.8 W/mm at 8 GHz [10]. Keller et al. provides a review of the development of the HEMT at UCSB[11].

Research publication time line for GaN FETs, HBTs, and conventional HBTs

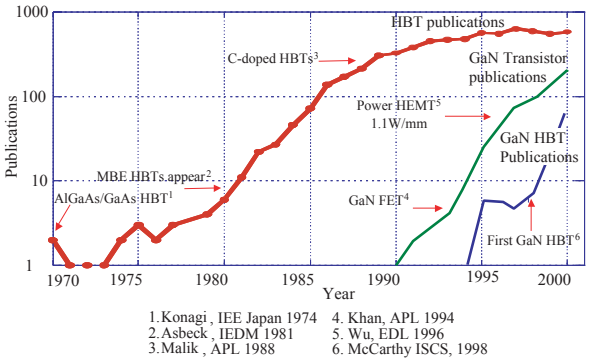

Figure 1.1: The number of INSPEC citations per year are shown in a semi-log plot for conventional HBTs, GaN transistors, and GaN HBTs. A few selected points of interest for this time line are indicated above.

The progress for HBTs began later, with the first reported AlGaN/GaN HBT in 1998 [12] (See § 3.2). Shortly following, two other groups reported HBT results, Yoshida et al. showing common emitter current gains over ten[13], Fan et al. [14] and Shelton et al. [15] also reported HBTs, but these devices could not be tested in the common emitter mode due to high leakage (see § 5.2.1). In 1999, Limb et al. reported HBTs using a selectively regrown emitter [16]. Other publications include the fabrication of an HBT on LEO GaN[17](see Chapter 5), and increased current gain HBTs grown by MOCVD using the regrown emitter technique[18]. The current gain and common emitter offset voltage of devices has been studied as a function of temperature by Huang et al.[19].

1.3 Synopsis of the dissertation

This dissertation covers several areas of research into the development of the AlGaN/GaN HBT in the pursuit of the fabrication of a device which could be tested at high frequencies. Although an RF device was the end goal, the majority of the effort was expended and understanding gained in the development process. Chapter 2 forms the foundation of the dissertation by introducing the particulars of the fabrication of the HBT. This includes the growth techniques and recipes as well as the resulting material properties and the fabrication techniques. Also discussed is the device structure as it was designed, and the moti-

[2] INSPEC® Institute of Electrical Engineers, UK.

vation for the design chosen. Polarization effects in the emitter were a consideration in the design of the HBT, and these are treated in § 2.4.1. Chapter 3 presents initial device results of the AlGaN/GaN HBT, and discusses one of the two most obvious symptoms of the low conductivity of the base layer and base contacts. The common emitter offset voltage is discussed as it relates to the base conductivity, and an explanation is given for a larger than expected offset voltage. Methods to reduce this offset voltage are also discussed, and some positive results given. Chapter 4 discusses the second major limitation on the performance of the HBT, the current gain. Several experiments were aimed at increasing the current gain, including the narrowing of the base layer, the change of aluminum composition in the emitter-base heterojunction, and aluminum compositional grading in the base. Emitter current crowding effects are discussed and proposed as a contributor to the gain limitations observed. Emitter-collector leakage was observed in several more lightly doped samples, and this is addressed in Chapter 5. The effect of this leakage on device characteristics is discussed, and methods for reducing this leakage are presented. Devices were fabricated on substrates grown using the lateral epitaxial overgrowth (LEO) technique, reducing dislocation densities in some areas. Collector-emitter leakage was measured as a function of dislocation density, and a proposed current path is discussed. Finally, in Chapter 6, the fabrication of transistors that can be probed using coplanar wave guide (CPW) on-wafer probes is presented, and the results of small signal S-parameter measurements are discussed. Once again the low conductivity of the base layer is found to be a dominant factor in the performance of the device, which is explained in § 6.3.3.

Due to the difficulties associated with the low conductivity of the base layer, and the poor contacts, the improvement of these aspects, both from a processing perspective as well as a growth perspective, remains central to the ongoing research into the AlGaN/GaN HBT. Although the ultimate goal of the research represented by this dissertation was to demonstrate the RF performance of AlGaN/GaN HBTs, much of the work, and much of the understanding gained, was exploratory in nature. It is hoped that what follows represents a sound beginning to the extensive work that lies ahead.

References

[1] U. V. Bhapkar and M. S. Shur. Monte carlo calculation of velocity-field characteristics of wurtzite gan. *J. Appl. Phys. (USA)*, 82(4):1649–55, 1997.

[2] J. Kolnik, I. H. Oguzman, K. F. Brennan, Wang Rongping, and P. P. Ruden. Monte carlo calculation of electron initiated impact ionization in bulk zinc-blende and wurtzite gan. *J. Appl. Phys. (USA)*, 81(2):726–33, 1997.

[3] Q. Lee, S. C. Martin, D. Mensa, R. P. Smith, J. Guthrie, S. Jaganathan, T. Mathew, S. Krishnan, S. Creran, and M. J. W. Rodwell. Submicron transferred-substrate heterojunction bipolar transistors with greater than 8000 ghz f/sub max. pages 175–8, 1999.

[4] G. b Gao and H. Morkoc. Material-based comparison for power heterojunction bipolar transistors. *IEEE Transactions on Electron Devices*, 38(11):2410–16, 1991.

[5] Peter Kozodoy. *Magnesium-doped gallium nitride for electronic and optoelectronic device applications*. PhD thesis, University of California, Santa Barbara, 1999.

[6] Z. Z. Bandic, P. M. Bridger, E. C. Piquette, and T. C. McGill. Electron diffusion length and lifetime in p-type gan. *Applied Physics Letters*, 73(22):3276–8, 1998.

[7] M. A. Khan, J. N. Kuznia, A. R. Bhattarai, and D. T. Olson. Metal semiconductor field effect transistor based on single crystal gan. *Applied Physics Letters*, 62(15):1786–7, 1993.

[8] S. C. Binari, L. B. Rowland, W. Kruppa, G. Kelner, K. Doverspike, and D. K. Gaskill. Microwave performance of gan mesfets. *Electronics Letters*, 30(15):1248–9, 1994.

[9] Y. F. Wu, B. P. Keller, S. Keller, D. Kapolnek, S. P. Denbaars, and U. K. Mishra. Measured microwave power performance of algan/gan modfet. *IEEE Electron Device Letters*, 17(9):455–7, 1996.

[10] Wu Yi-Feng, D. Kapolnek, J. P. Ibbetson, P. Parikh, B. P. Keller, and U. K. Mishra. Very-high power density algan/gan hemts. *IEEE Transactions on Electron Devices*, 48(3):586–90, 2001.

[11] S. Keller, Wu Yi-Feng, G. Parish, Ziang Naiqian, J. J. Xu, B. P. Keller, S. P. DenBaars, and U. K. Mishra. Gallium nitride based high power heterojunction field effect transistors: process development and present status at ucsb. *IEEE Transactions on Electron Devices*, 48(3):552–9, 2001.

[12] L. S. McCarthy, P. Kozodoy, M. J. W. Rodwell, S. P. DenBaars, and U. K. Mishra. Algan/gan heterojunction bipolar transistor. *IEEE Electron Device Letters*, 20(6):277–9, 1999.

[13] S. Yoshida and J. Suzuki. High-temperature reliability of gan metal semiconductor field-effect transistor and bipolar junction transistor. *Journal of Applied Physics*, 85(11):7931–4, 1999.

[14] Ren Fan, C. R. Abernathy, J. M. Van Hove, P. P. Chow, R. Hickman, J. J. Klaasen, R. F. Kopf, Cho Hyun, K. B. Jung, J. R. La Roche, G. Wilson, J. Han, R. J. Shul, A. G. Baca, and S. J. Pearton. 300 degrees c gan/algan heterojunction bipolar transistor. *MRS Internet Journal of Nitride Semiconductor Research*, 3, 1998.

[15] B. S. Shelton, J. J. Huang, D. J. H. Lambert, T. G. Zhu, M. M. Wong, C. J. Eiting, H. K. Kwon, M. Feng, and R. D. Dupuis. Algan/gan heterojunction bipolar transistors grown by metal organic chemical vapour deposition. *Electronics Letters*, 36(1):80–1, 2000.

[16] J. B. Limb, L. McCarthy, P. Kozodoy, H. Xing, J. Ibbetson, Y. Smorchkova, S. P. DenBaars, and U. K. Mishra. Algan/gan hbts using regrown emitter. *Electronics Letters*, 35(19):1671–3, 1999.

[17] L. McCarthy, I. Smorchkova, H. Xing, P. Fini, S. Keller, J. Speck, S. P. DenBaars, M. J. W. Rodwell, and U. K. Mishra. Effect of threading dislocations on algan/gan heterojunction bipolar transistors. *Applied Physics Letters*, 78(15):2235–7, 2001.

[18] H. Xing, L. McCarthy, S. Keller, S. P. DenBaars, and U. K. Mishra. High current gain gan bipolar junction transistors with regrown emitters. *2000 IEEE Symposium on Compound Semiconductors.* pages 365–9, 2000.

[19] J. J. Huang, M. Hattendorf, M. Feng, D. J. H. Lambert, B. S. Shelton, M. M. Wong, U. Chowdhury, T. G. Zhu, H. K. Kwon, and R. D. Dupuis. Temperature dependent common emitter current gain and collector-emitter offset voltage study in algan/gan heterojunction bipolar transistors. *IEEE Electron Device Letters*, 22(4):157–9, 2001.

2

Design and fabrication of the AlGaN/GaN HBT

2.1 Introduction

THE fabrication of the AlGaN/GaN HBT can be subdivided into two principal components. First, the AlGaN/GaN device must be grown, and secondly, it must be processed to contact the device layers, the emitter, base, and collector. Owing to the relative immaturity of the III-N material system, neither aspect is straightforward. This chapter describes in some detail both the growth and processing of the AlGaN/GaN HBT.

Although all aspects of device processing were performed by myself, the growths for the transistors were performed by several individuals on various growth systems using two principal growth techniques: Metal Organic Chemical Vapor Deposition (MOCVD) and Molecular Beam Epitaxy (MBE). The two techniques are substantially different, and both are discussed below. Growths by MOCVD were performed by Peter Kozodoy, Paul Fini, Huili Xing, and Brendan Moran, while growths by MBE were performed by Ioulia Smorchkova.

After the devices were grown, they were processed in the UCSB co-search cleanroom. Facilities used included, among others, an RTS inc. modified GCA I-line wafer stepper, PlasmaTherm RIE and PECVD tools, and a Temescal e-beam evaporator. The development of the fabrication process of the AlGaN/GaN HBT was a central goal to this study, and as such it changed considerably throughout the research. In general, only the final generation of this process is presented, although several alternatives were explored with varying success.

This chapter is arranged in two parts to reflect the two-part growth / process procedure, and arranged in the order of actual use in the fabrication of the devices. In this chapter, only the process and growth steps for the basic device are presented. Also presented are the considerations that went into the design of the device. Growth and fabrication which is particular to specific experiments is presented in later chapters with those experiments. Finally, some of the more significant process improvements are presented.

2.2 Growth of AlGaN/GaN transistor structures

Initial studies of the AlGaN/GaN bipolar transistors at UCSB were performed on devices fabricated on material grown entirely by Metal Organic Chemical Vapor Deposition (MOCVD) on sapphire substrates. In much of the later work which is represented by the bulk of this dissertation, the devices were fabricated using a combination of MOCVD and MBE. The reason for the change will be discussed later in this chapter.

Due to the large crystal lattice mismatch between GaN and sapphire, much of the GaN crystal growth is dedicated to creating a high quality single crystal template on which active device layers can be grown homoepitaxially. The availability of multiple MOCVD reactors allowed for a variety of sources for these templates, and therefore a variety of growth conditions and procedures for various templates. Generally, these templates were considered as equivalent. It should also be noted that the HBT structure did not lend itself to direct measurements of film thickness, dopant concentration and other material characterization tools. For this reason, much of the data gathered was indirect – calibration structures were typically grown to investigate particular layers, or calibrate growth rates. These growth rate calibrations and doping calibrations were then used to inform the growth of the active layers. The material characteristics presented below: Doping concentrations, material thickness and mobility measurements etc. are generally taken from materials research on the same machine under similar conditions and assumed to be valid approximations for material characteristics of device structures.

2.2.1 MOCVD growth: Experimental setup

The following description of the typical growth conditions for MOCVD growth on a particular machine is generally representative of the growth techniques used on the other machines as well. MOCVD growth was used for active layers, templates for MBE active layers, and special lateral epitaxial overgrowth templates for MBE active layers with reduced threading dislocation densities. For a more complete description of these growth techniques, in depth discussions can be found in the Ph.D. dissertations of Peter Kozodoy [1] (specifically regarding Mg doped layers), and Paul Fini [2] (specifically regarding Lateral Epitaxial Overgrowth, (LEO), layers) , as well as publications by S. Keller et al. [3] and others [4, 5] regarding general template growth.

The following excerpt from Peter Kozodoy's Ph.D. dissertation [1] describes the growth conditions he used for these growths and is representative of all other vertical (non LEO) MOCVD growths performed for devices described here.

> . . . Growths were performed on a modified Thomas Swan MOCVD growth machine at UCSB. This is a horizontal quartz reactor with separate group V and group III input flows. Designed in order to

reduce pre-reactions, the wafer is held in a graphite susceptor and the growth temperature is measured using a thermocouple placed within the susceptor. The pressure during the growth may be controlled between atmosphere and approximately 30 Torr. during typical GaN growth conditions, the gas ambient is composed primarily of NH_3, in addition to H_2 and N_2 (usually mainly H_2). All of these gasses are purified before entering the growth chamber. The metalorganic sources used are trimethylgallium (TMGa), trimethylaluminum (TMAl), trimethylindium (TMIn), and biscyclopenntadienyl-magnesium (Cp_2Mg). Silicon doping is accomplished with a gas source of dilute disilane in H_2. *From the dissertation of Peter Kozodoy, UCSB Pg 29*[1]

2.2.2 MOCVD Template Growth

Growth was performed on *c*-plane sapphire substrates, which were etched in a high temperature (1050°C) H_2 step prior to nucleation layer deposition[1]. The low temperature nucleation growth is followed by a higher temperature (1070 °C) growth for the remainder of the GaN template; the two layer nucleation process effecting the defect structure within the films[6]. The conditions for this heteroepitaxial growth were developed primarily by Bernd Keller, Dave Kapolnek, and Stacia Keller [4, 5, 7]. Table 2.1 shows a sample of growth conditions for a template growth.

Layer	Thickness [nm]	Temp [°C]	Press [Torr]	NH_3 [L/min]	TMGa [sccm]
LT GaN	20	525	770	6	31.1
GaN	1000	1065	770	6	26.1
GaN	500	1065	770	6	13.1

Table 2.1: Sample growth conditions for template growth in Lateral modified Thomas Swan reactor.

2.2.3 Active layer growth by MOCVD

Silicon doping is added during MOCVD growth to produce the n-type material for the emitter and subcollector layers of the npn transistor. Disilane flows of approximately 0.4 sccm were shown by Hall measurements to have an electron concentration of 5×10^{18} cm^{-3} with a mobility of 300 cm^2/Vs[6]. For these structures, the emitter and subcollector layers both were doped approximately 5×10^{18} cm^{-3}.

Magnesium doping was used to create the p-type base layer for the npn bipolar transistor. The initial work in the development of the processing and MOCVD growth technologies for p-type layers at UCSB was performed principally by Peter Kozodoy [1], who provided all of the MOCVD grown active device layers. The p-type base layers for these devices were typically grown to a thickness between 100 nm and 200 nm. It should be noted, however, that due to large growth rate non-uniformity in this reactor, the precise thickness of the layers was uncertain. Table 2.2 shows typical growth conditions for the active layers of a device. This structure is further discussed in § 2.4

Layer	d [nm]	Temp [°C]	Press [Torr]	NH_3 [L/min]	TMGa [sccm]	TMAl [sccm]	DiSi [sccm]	Cp_2Mg [sccm]
GaN:Si	2000	1065	770	6	26.1		0.8	
GaN	750	1070	770	6	26.1			
GaN:Mg	100	1000	770	6	6.53			11.5
AlGaN:Si	15	1050	200	6	2.95	1.97	0.2	
GaN:Si	15	1050	200	6	3.27		0.2	

Table 2.2: Sample growth conditions for active layer growth by MOCVD in Lateral modified Thomas Swan reactor.

2.2.4 Homoepitaxial MBE Growth

MBE grown active device layers for this study were grown by Ioulia
Smorchkova at UCSB. The process for the growth of HBT active layers was similar to the methods described in (*Smorchkova et. al. JAP 1999*)[8]:

> Structures have been grown by rf plasma-assisted molecular-beam epitaxy. The growth was performed in a Varian Gen II MBE system. Active nitrogen for growth was supplied by an EPI Unibulb nitrogen plasma source utilizing ultra-high-purity nitrogen (99.9995%), which was further purified by an inert gas purifier (Aeronex, San Diego, CA) installed at the rf plasma source gas inlet. Elemental Ga (6N) and Al (6N) supplied from conventional effusion cells were used for the group III sources. Unintentionally doped GaN templates grown on (0001) sapphire by atmospheric pressure MOCVD were used as substrates for the MBE growth of the AlGaN/GaN structures. Prior to introduction into the MBE system, the templates were cut into ∼10mm × 10mm pieces, cleaned using acetone, methanol, and isopropanol, and mounted on EPI Uniblock molybdenum sample holders. These holders were then loaded into the MBE buffer chamber where they were baked at 450°C for 60 min before the growth to remove residual moisture. The substrate temperature during the growth was monitored using an optical pyrometer focused on a titanium film deposited on the back of the template. The purpose of this Ti layer was to provide an efficient heat transfer from the substrate heater to the sample. The growth was performed at ∼750°C with a high III/V flux ratio. (*From Smorchkova et. al. JAP 1999. pp 4521* [8])

The MBE growth process described above is slower than the MOCVD process – growth rates were approximately 0.2 μm/hour. The Mg doped GaN is grown at lower temperatures, ∼650°C to facilitate Mg incorporation, and results in a high quality GaN:Mg film with carrier concentrations as high as 1.4×10^{18} cm^{-3} with a mobility of 7.5 cm^2/Vs[9]. Due to the more reproducible nature of the MBE growth (relative to the

MOCVD reactor described above) the layer thickness and doping concentrations could be known to a greater degree of accuracy. It should be noted, however, that temperature was difficult to control by MBE and this may have affected the Mg incorporation in the film. Table 2.3 represents typical HBT growth parameters for the active layers of an HBT structure. The table shows a sample set of growth conditions for the active layers grown by MBE for an HBT growth. Nitrogen pressure was held at 1.7×10^{-5} Torr, with the RF source at 150 Watts. Not shown are the grading steps for the Al barrier in the emitter. The growth is on an MOCVD template which already incorporates the subcollector and a portion of the not-intentionally-doped collector.

				Source emission			
Layer	Time [min]	Substrate [°C]	N_2 [μTorr]	Ga [μTorr]	Al [μTorr]	Mg [μTorr]	Si [°C]
GaN	65	652	11	0.218			
GaN:Mg	35	652	11	0.218		0.0025	
$Al_{0.1}Ga_{0.9}N$:Si	18.5	652	11	0.218	0.0157		1240
GaN:Si	20	652	11	0.218			1240

Table 2.3: MBE Growth of active layers. Source emission pressures are the beam emission pressure as measured before growth with an ion gauge at the wafer plane.

2.3 Material properties

2.3.1 MOCVD grown templates

The undoped template films have a background ionized donor concentration "on the order of n=4×10^{16} cm^{-3}, mobilities as high as 820 cm^2/Vs, typical x-ray diffraction peak widths of 270 on-axis (002) and 390 off-axis (102), and threading dislocation density between 10^8 and 10^9 cm^{-2}, as measured by transition electron microscopy (TEM)" [1]. The background concentration is thought to be due to oxygen contamination as well as donor-like point defects such as nitrogen vacancies in the films. Threading dislocations generally propagate vertically through the structure, and are annihilated only through thick growths, novel nucleation techniques, or lateral epitaxial overgrowth (LEO). When MBE layers are grown on these dislocated templates, the dislocations are typically incorporated into the MBE layers such that the dislocation density observed in the active MBE layers is generally similar to that of the template on which it is grown[10].

2.3.2 p-type (Mg doped) GaN

Properties which are common to both MOCVD and MBE p-type films include the acceptor ionization energy, issues with compensation of films, low hole mobilities, and difficulties with contacting etched as well as the as-grown layers. Magnesium is a deep acceptor, $E_A - E_V \approx 110-200$ meV [11], resulting in a carrier concentration of p=8×10^{17} cm^{-3} for an acceptor density of $\sim 1\times10^{19}$cm^{-3}. Although there are reports of higher hole concentrations using co-doping of Mg with oxygen or silicon[12], electronic device results with this doping technology have not been reported. Holes in GaN, with an effective mass of 2.2$\cdot$ m_0[13], had mobilities between 5 and 20 cm^2/V s in highly doped GaN:Mg layers. In addition, both MOCVD and MBE films are degraded by compensation effects in the films. The result is material with a resistivity on the order of 1 $\Omega\cdot$cm.

Another critical characteristic of p-GaN layers is the minority carrier diffusion length of the bulk material. Unfortunately this research is in preliminary stages for p-type films and reports vary. Much of the variation in reports is likely due to a wide variation in material grown by different groups. Groups have reported values of $\sim$200 nm for films with hole concentrations around p = 2.5×10^{17} cm^{-3}[14, 15]. Smaller numbers were reported for a production-like LED structure by Gonzalez et al. [16] who reported diffusion lengths in a p-layer of 80 nm (the acceptor concentration was not mentioned). Further complicating the issue is the apparent spread in material characteristics grown by different research groups. This may be due to different Mg doping concentration, different levels of impurities, overall crystal quality, etc. It is likely, however, that the diffusion length is on the order of the base width, which would be expected to limit the current gain. Also notable is the report of a lower diffusion length (55 nm) for Mg doped $Al_{0.1}$GaN [16]. The implication here is that the advantages gained by bandgap grading in the base using aluminum mole fraction may be reduced (Chapter 4).

2.3.3 MOCVD vs. MBE grown material

Of particular interest is the difference between p-type layers and p-n junctions grown by MOCVD and MBE. When grown in a hydrogen ambient, as the MOCVD films typically are, the Mg acceptor is passivated by the hydrogen and must be thermally activated before devices are operable[17]. The anneal used for these experiments is discussed with the rest of the process flow in section § 2.5. Although the anneal is effective in activating the acceptors in a sample, the activation efficiency is less than 100%. MBE grown films, conversely, are not grown in a hydrogen ambient, and therefore are not passivated during growth. The result is a film which does not need to be activated. Also, MBE films with similar carrier concentrations to their MOCVD counterparts had higher mobilities, suggesting that the MBE films may have either fewer unintentional impurities or higher activation efficiency, reducing scattering rates for the holes. An important factor in HBT growths is the emitter-base heterojunction placement. A secondary ion mass spectroscopy (SIMS) measurement was used to determine the sharpness of the emitter-base junction grown by MOCVD and MBE. Figure 2.1 shows the broadening of the Mg profile grown by MOCVD. Both the MBE and MOCVD films were intended to have abrupt junctions with layers of approximately the same width. The slower turn-off of Mg in the case of the MOCVD grown structure may be due to memory effects or higher impurity diffusion rates associated with higher growth temperatures. Any memory effect would also be expected to depend strongly on reactor design and growth conditions. At

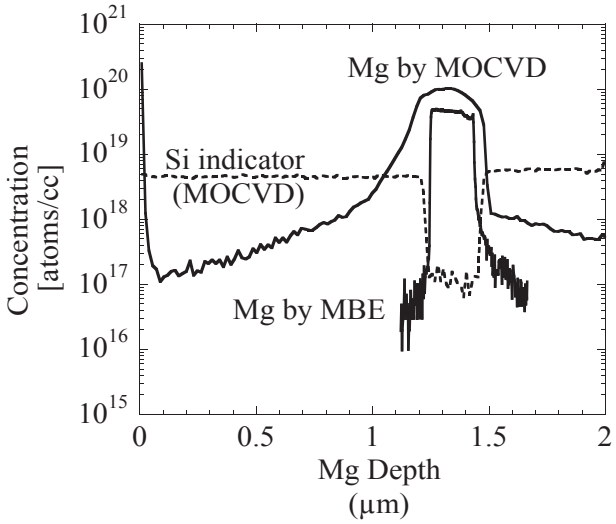

Figure 2.1: The SIMS profile indicates a significant widening of the MOCVD grown layer, in contrast to a very abrupt metallurgical junction in the case of the MBE grown films. The Si doping profile in the MOCVD layer indicates the inverse of the intended Mg doping profile. *(MOCVD SIMS data courtesy of P. Kozodoy[1], MBE SIMS data courtesy of I. Smorchkova)*

the time of this dissertation, however, little had been published regarding the material quality of the GaN:Mg layers grown by MBE [9]. The majority of the experiments grown for this dissertation were grown by MBE due to a higher degree of control of junction placement, and better uniformity across the wafer. Minority carrier lifetimes in p-type layers were unknown for either of the two growth techniques.

2.3.4 Polarization effects

The polarization charge (P) consisting of spontaneous (P_{SP}) as well as piezoelectric (P_{PZ}) components, significantly effects many devices on III-N films, and must therefore be considered in the design structures including alloys to GaN. The strong polarity of the wurtzite GaN crystal, combined with the large lattice mismatch between GaN and its aluminum alloys results in structures which are subject to polarization charge on the order of typical doping concentrations. The total polarization charge in pseudomorphic AlGaN layers as a function of the change in aluminum mole fraction, δx, is the sum of the spontaneous and piezoelectric polarization charges: $[P_{SP}(\delta x) + P_{PZ}(\delta x)]$ and can be written:

$$P(\delta x) = P_{SP}(\delta x) + 2\left(e_{31} + \frac{c_{13}}{c_{33}}\, e_{33}\right) E(\delta x) \qquad (2.3.1)$$

where $E(\delta x)$ is the unit less in-plane strain of the pseudomorphic AlGaN layer and calculated by linearly interpolating from the binaries, AlN and GaN[18].

$$E(\delta x) = \frac{a' - a(\delta x)}{a} = 0.0241\delta x \qquad (2.3.2)$$

where a and a' are the relaxed and strained lattice constants respectively. The spontaneous and piezoelectric polarization constants, e_{31} and e_{33} [19] as well as the elastic constants, c_{13} and c_{33}[20] can also be linearly interpolated from binary values. Table 2.4 shows the linear interpolation of these constants between the binaries (GaN and AlN). As can be seen from this table, the effect of aluminum composition on the piezoelectric and elastic coefficients for small variations, $(x < 10\%)$ is relatively small, allowing the use of an average values for graded layers. Even for dilute alloy changes (10%), the polarization charge results in sheet charge concentrations on the order of 10^{-6} C/cm^2. The concentration of this charge can be reduced by changing alloy composition gradually. The effects of polarization charge on device structures is discussed in § 2.4.1

Constant	Value (x)	Units
$P_{SP}(\delta x)$	$-0.052(\delta x)$	[C/m^2]
$e_{31}(x)$	$-0.49 - 0.11(x)$	[C/m^2]
$e_{33}(x)$	$0.73\,(1 + x)$	[C/m^2]
$c_{13}(x)$	$103 + 5(x)$	[GPa]
$c_{33}(x)$	$405 - 27(x)$	[GPa]
$a(x)$	$0.3189 - 0.0077(x)$	[nm]

Table 2.4: Table of values used for calculating polarization charge in $Al_xGa_{1-x}N$ films.

2.4 Structure

A typical device structure used in these experiments along with a simulated band diagram[1] under bias is shown in Figure 2.2. The emitter was $Al_{0.1}Ga_{0.9}N$:Si (N_D=5×10^{18} cm^{-3}) with a GaN:Si emitter contact layer. The base layer was 100 nm GaN:Mg, N_A=5×10^{19} cm^{-3}. The collector was 500 nm unintentionally doped (UID) GaN with a background donor concentration of 5×10^{16} cm^{-3}. The subcollector was GaN:Si, N_D=×10^{18} cm^{-3}. Although the structure shown here had its active layers grown by MBE, it is also substantially representative of the devices where active layers were grown by MOCVD.

[1] This and subsequent band diagram simulations were performed using *BandProf* written by William R. Frensley, (C) Copyright the University of Texas at Dallas, Feb. 15, 1991. http://www.utdallas.edu/ frensley/hlts/bandprof.html. Material constants were taken from published values for GaN and AlN, with alloy material constants linearly interpolated from the binaries.

Device Structure and band diagram

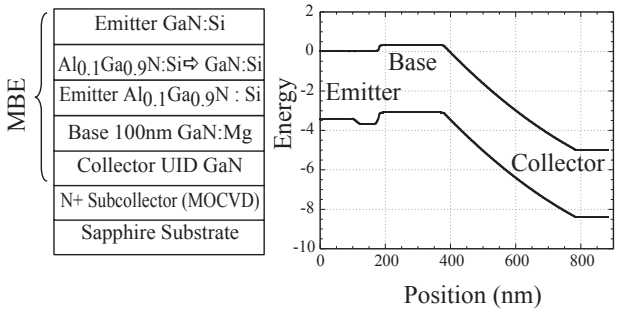

Figure 2.2: **Left:** Typical structure for AlGaN/GaN HBT grown by plasma assisted MBE on MOCVD GaN on sapphire.
Right: Simulated band diagram of typical device. The $Al_{0.1}Ga_{0.9}N$ heterojunction provides a barrier to hole injection into the emitter.

2.4.1 Emitter design

The emitter for the HBT was designed to provide sufficient barrier to hole injection in forward bias without compromising the vertical electron conductivity. Chapter 4 discusses the emitter injection efficiency (§ 4.2.1) in greater detail, but some of the relationships are repeated here for convenience.

For graded heterojunctions the thermionic barrier in the conduction band at the heterojunction is reduced, and current flow is related to voltage in much the same way as in the homojunction case. The key difference, afforded by the larger bandgap in the emitter, is a lower equilibrium minority carrier concentration in the emitter. This allows for the design of emitter-base junctions where the emitter doping may be decreased to reduce junction capacitance, and the base doping increased to reduce output conductance and bulk base resistance. In conventional III-V HBTs (which typically use graded heterojunctions), the base current due to the injection of holes into the emitter can be written as:

$$I_{B_P} = \frac{qA_E D_{pE}}{X_E} \frac{n_{iE}^2}{N_E} \exp\left(\frac{qV_{BE}}{kT}\right) \qquad (2.4.1)$$

Where A_E is the emitter area, D_{pE} the diffusion length of holes in the emitter, X_E the extent of the depletion region in the emitter, n_{iE}^2 the intrinsic carrier concentration in the emitter, N_E the active carrier concentration in the emitter, and V_{BE} is the applied junction bias[21]. Equation 2.4.1 shows that the back-injected current is proportional to n_{iE}^2. The intrinsic carrier concentration is related to the band gap by:

$$n_i^2 = N_C N_V \exp\left(-\frac{E_G}{kT}\right) \qquad (2.4.2)$$

where N_C and N_V are the conduction and valence band density of states respectively. Thus, increasing the bandgap in the emitter for a graded heterojunction reduces back injection into the emitter by a factor of $\approx \exp(\Delta E_g/kT)$. The bandgap ($E_g$) of $Al_{0.1}Ga_{0.9}N$ is estimated using a linear interpolation of bandgap from AlN (6.2 eV) to GaN(3.4 eV) to have a bandgap of ∼3.7 eV or about 10 kT (at room temperature) greater than the bandgap of GaN (3.4 eV). Assuming approximately the same donor ionization energy as for GaN, this leads to a reduction of $\approx \exp(10)$ in hole injection.

Polarization effects and emitter design

As discussed in § 2.3.4, polarization effects must be considered in the design of structures with changing alloy compositions, such as the emitter in the HBT. Figure 2.3 shows simulated band diagrams of the base-emitter diode of an abrupt $Al_{0.1}GaN$ /GaN heterojunction with and without consideration of polarization charge. As can be seen from this figure, the polarization acts

Abrupt N-p junction band diagrams

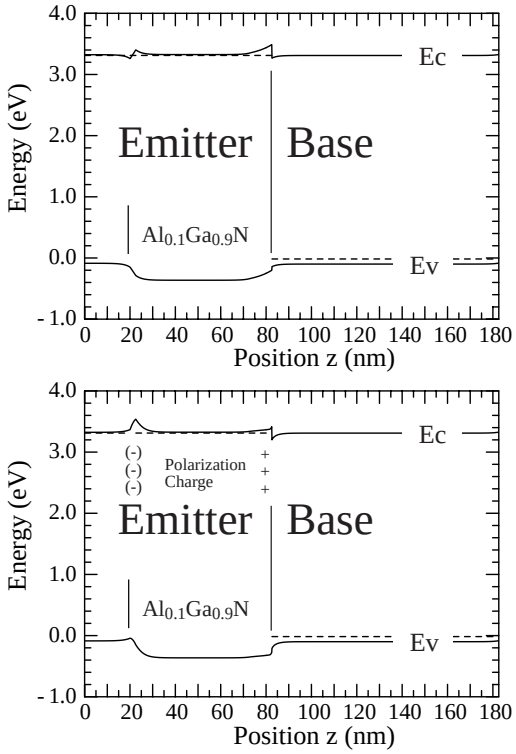

Figure 2.3: Simulated band diagrams of abrupt N -p $Al_{0.1}GaN$: Si(5×10^{18} cm^{-3}) /GaN : Mg (p=1×10^{18} cm^{-3}) emitter-base heterojunction forward biased to flatband without (**Above:**) and with (**Below:**) polarization effects. The dip in the valence band and corresponding notches in the conduction band are coincident with the $Al_{0.1}GaN$ layer.

to "pull down" the conduction band at the emitter-base heterojunction with a positive or donor-like sheet charge, but increases the barrier at the GaN/$Al_{0.1}GaN$ interface within the emitter with

a negative or acceptor-like sheet charge. For a change in Al composition of 10%, the charge density can be calculated from Equation 2.3.1 to be $\sim 6\times10^{-7}$ C/cm^2. To reduce the barrier in the conduction band and maximize the valence band barrier at the base-emitter heterojunction, the alloy composition of the emitter was graded both at the base-emitter heterojunction interface, and at the hetero-interface within the emitter (Figure 2.4).

Graded N-p junction band diagrams

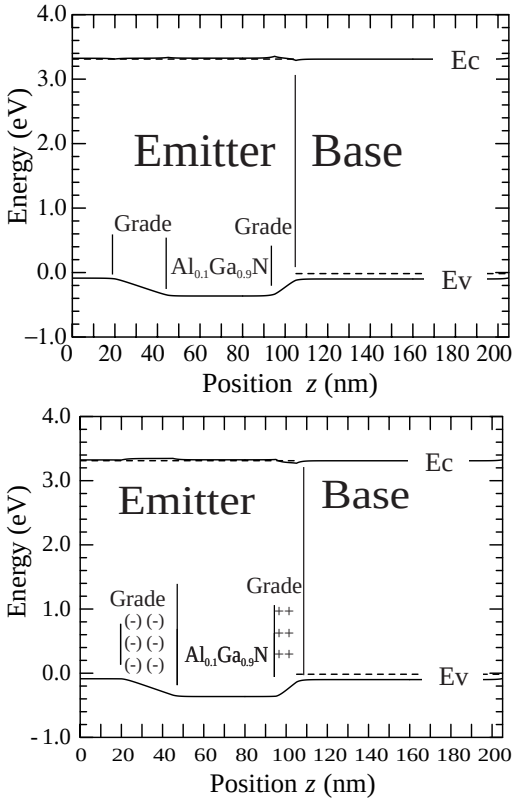

Figure 2.4: Simulated band diagrams as in Figure 2.3 but with the aluminum composition graded over 10 nm at the base-emitter heterojunction and over 25 nm at the heterojunction within the emitter.
Above: Band diagram simulation without polarization charge. **Below:**With polarization charge.

The entire emitter was doped $\sim5\times10^{18}$ cm^{-3} Si. From the top of the emitter towards the collector, the emitter cap contact layer was 15 nm of GaN, with a grade in of Al to 10% over 25 nm. The grade here is to avoid an abrupt barrier in the conduction band of the emitter. Comparing Figure 2.4 with Figure 2.3 shows the reduction of the conduction band barrier accomplished with the grade in. The grading spreads out the polarization charge resulting in an acceptor-like charge concentration of $-q\cdot 2\times10^{18}$ C·cm^{-3}. Figure 2.5 shows a detailed view of the conduction band in the band diagram simulation from Figure 2.4.

Even with the grading, the polarization effects associated with the changes in Al composition limited the design to relatively dilute alloys and strong emitter doping. Fortunately, as discussed above, these alloys provided for a significant change in the bandgap ($\sim10kT$) which was assumed to be sufficient to substantially prevent the back-injection of holes.

Simulated band diagram showing the conduction band of the HBT with polarization effects in a graded structure

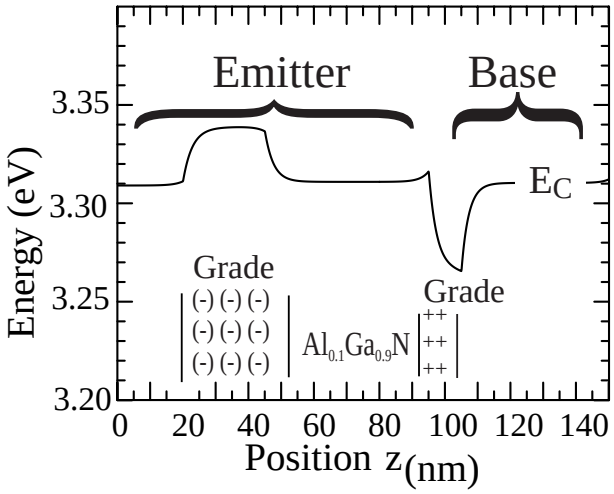

Figure 2.5: The simulated band diagram shows the conduction band barrier caused by the reduction in aluminum concentration. 10% Al is graded down over 25 nm leading to a polarization charge equivalent to an acceptor concentration of $\sim2\times10^{18}$cm^{-3}. The Si emitter doping was 5×10^{18}cm^{-3}. The polarization charge leads to a barrier in the conduction band of about kT.

2.4.2 Base design

The base layer of the transistor structure was doped as strongly as possible ($N_A \sim 5\times10^{19}$ cm^{-3}) to minimize the lateral resistance in the base. Originally the base was designed to be 200 nm when grown by MOCVD with a design change for MBE structures that reduced the thickness to 100 nm. The change was made because, with the non-uniformity of the base layers grown by MOCVD, it was believed that the working devices on those layers most likely had thinner-than-designed emitters. Ideally, to maximize gain (at the cost of base conductivity), the base layer may be designed as thin as possible to maximize base transport efficiency. As discussed in § 2.3.2, the diffusion length of electrons in the base (L_n) was expected to be on the order of

100 nm. Typically, the base width (W_B) is designed such that $W_B << L_n$. Practical issues, however, necessitated a thicker layer. The low conductivity of the base material limited the design of the base thickness. Even with the thicker base, the base sheet resistance was expected to be between 50 and 150 k$\Omega/\square$. The gain of these devices as a function of base width is discussed in Chapter 4. Also, because the emitter mesa etch was non-selective , to reliably etch to the base without punching through to the collector, the minimum usable base thickness was found to be about 75 nm.

2.4.3 Collector and subcollector

In a conventional HBT, the collector is designed to be fully depleted under normal bias conditions, with a subcollector forming the contact layer. Electrons transit vertically through the collector region, and laterally in the subcollector to the collector contacts. The collector design was perhaps the least critical to these studies, as it is generally relevant to the breakdown voltage - electron transit time (τ_C)trade off. We needed an adequate breakdown (preferably $>$ 40V) without unnecessarily increasing collector thickness, but the focus of these studies was not to maximize the breakdown, or even minimize the electron transit time. Figure 2.2 shows such a design. Collectors were grown unintentionally doped, which resulted in a background donor concentration between 5-10$\times 10^{16}$ cm^{-3}. The collector layer was $\sim$500 nm. The subcollector was thicker, usually 750-1000 nm doped with Si, N_D=5$\times 10^{18}$ cm^{-3}. Typically, the subcollector and part of the collector were included in the MOCVD template for growths where the active layers were grown by MBE. It will be shown later (Chapter 6) that the dominant limitation on RF performance for these devices was likely elsewhere.

2.5 Device processing

2.5.1 General process considerations

Devices were fabricated using Cl_2 Reactive Ion etching (RIE), metal evaporation and liftoff. An illustration of the fabrication process is shown in Figure 2.6. For devices fabricated from active layers grown by MOCVD, a p-type activation anneal was required, and was performed before any other processing. The thermal activation process was first published by Nakamura et al. [17] and developed for UCSB by Kozodoy [1]. The process consisted of a 100 nm SiO_2 cap deposited by plasma enhanced chemical vapor deposition (PECVD) and a subsequent anneal for 3 minutes in an N_2 ambient at 950°C. The SiO_2 was then removed with buffered hydrofluoric acid (BHF). The following description is for the process flow for a typical DC device. Other special process sequences were developed for the fabrication of the RF compatible device, and the regrown base device and are discussed later.

Process flow

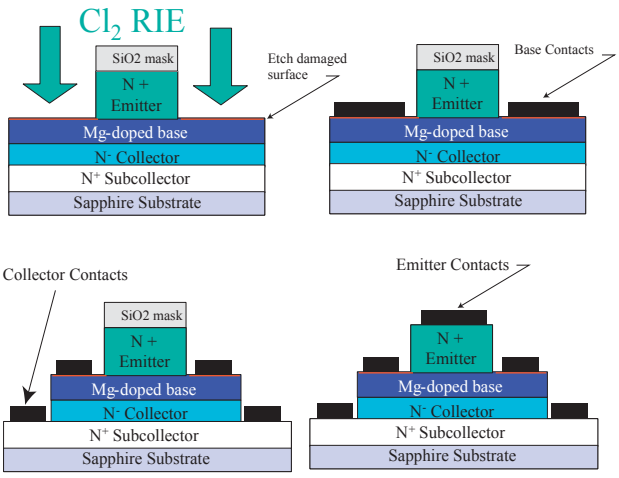

Figure 2.6: Process flow for HBT.

2.5.2 Emitter mesa etch

The Cl_2 RIE emitter mesa etch was controlled by time, and the access to the base layer was confirmed using a probe tip to test the polarity of the surface Schottky diode. The etch was performed in a PlasmaTherm shuttle-lock RIE tool modified with an adjustable electrode separation, high conductivity chamber and clamped backside helium cooling. The etch was performed on samples placed on 4 inch Si carrier wafers coated with PECVD SiO_2. The etch chemistry used Cl_2 gas flowing at 30 sccm held at a pressure of 10 mTorr and energized in RIE mode with a power of between $\sim$ 12 and 60 watts corresponding to a DC self-bias of between 2 and 120 V. Several emitter mesa etch masks were studied, the most effective was found to be $\sim$100 nm of evaporated SiO_2. This mask led to the cleanest etched surface (as determined visually from SEM micrograph) and benefited from high etch selectivity. It was also preferable to photo-resist as it did not need to be removed until emitter contacts were applied, providing valuable contrast for base contact alignments.

2.5.3 Base contact metalization

After the emitter mesa was etched, revealing the base layer, the base contacts were applied by metal evaporation and liftoff. Kozodoy showed that an optimum contact metalization for p-contacts was Pd/Au [1]. Initial contacts were made using the lithography procedure he developed. Kozodoy's method utilized the properties of the image reversal photo-resist to circumvent the conventional oxygen plasma descum which was found to degrade contacts to p-type material. Later, with the incorporation of stepper lithography that utilized positive photo-resist, a new alternative to the oxygen descum needed to be developed. The

Pd/Au/Pt contact was developed to this end. First Pd/Au (20/100 nm) was blanket deposited by evaporation. Next, photoresist was patterned for lift-off, and 100 nm of Pt was evaporated on the Pd/Au stack. After excess Pt was removed with the photoresist, the remaining Pt was used as a wet etch mask and the field metal (Pd/Au) was removed using an iodine based Au etchant.

2.5.4 DC device completion

After the base metalization, the base mesa was defined using a timed Cl_2 RIE etch. This etch used the same chemistry, but at a lower pressure (5 mTorr) and at higher power (200 Watts, 350V). This etch quickly reached the collector layer, to which collector contacts are applied. Next, the emitter mesa mask was removed in BHF, and photoresist was patterned for emitter and collector ohmic contacts simultaneously. The same metal stack, evaporated Al/Au (200 / 100 nm), was used for both the emitter and collector ohmic contacts.

After devices were fabricated, DC electrical testing was performed to characterize the devices. Primarily, common emitter DC characteristics and Gummel plots were used to evaluate experiments. Additional structures such as transfer length measurement (TLM) pads, large diodes, etc. were included to provide additional information as necessary. Typically, on devices with MOCVD active layers, device yields were quite low. Much of the time only a small area of the device wafer held working devices. Wafers where the active layers were grown by MBE were much smaller, (usually 1 cm^2), but often had working devices over a larger area.

2.5.5 Device geometries

Figure 2.7 shows the layout geometry and typical dimensions used in the experiments. Geometries for these preliminary device studies were chosen to be eventually compatible with RF characterization (Chapter 6). Also, in consideration of the high degree of anticipated emitter crowding, small emitter finger widths (W_E) were chosen. Conversely, the additional fabrication steps required to contact devices for RF probing were considerable, and so most device wafers were not processed past the DC stage. For this reason, it was a prerequisite that emitter fingers be large enough to be probed by conventional DC needle probes. This set the minimum emitter contact width to 1 μm. Also, initial devices were fabricated using contact lithography, which severely limited device dimensions and alignment tolerances. Various device sizes were fabricated, with emitter widths ranging from 1 to 5 μm, and lengths from 20 to 100 μm.

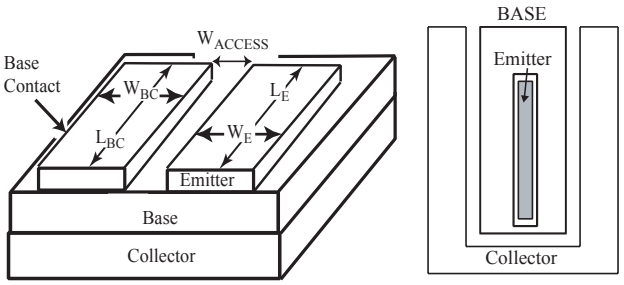

Figure 2.7: Diagram of the device geometry for the AlGaN/GaN HBT Device dimensions are as follows (in microns): W_E =3, L_E = 50, W_{Access} = 1, W_{BC} = 9, W_{BCX} = 8, L_{BC} = 72.

2.6 Summary

Fabrication procedures including template growth, active layer growth by MOCVD and active layer growth by MBE were introduced. Typical growth conditions were also given. Basic material properties relevant to the AlGaN/GaN HBT were introduced, including p-dopant (Mg) thermal activation, ionization energy, etc. Polarization effects on dilute alloys of AlGaN were discussed, and applied to a typical structure used in these experiments. That structure was presented, along with the motivation for specific design decisions. The basic relationship between emitter alloy composition and hole injection into the neutral emitter is discussed. The foundation for the device processing used in these studies is presented, and typical device geometries given.

References

[1] Peter Kozodoy. *Magnesium-doped gallium nitride for electronic and optoelectronic device applications.* PhD thesis, University of California, Santa Barbara, 1999.

[2] Paul T. Fini. *Threading dislocation reduction in gallium nitride thin films on sapphire via lateral epitaxial overgrowth.* PhD thesis, University of California, Santa Barbara, 2001.

[3] S. Keller, Wu Yi-Feng, G. Parish, Ziang Naiqian, J. J. Xu, B. P. Keller, S. P. DenBaars, and U. K. Mishra. Gallium nitride based high power heterojunction field effect transistors: process development and present status at ucsb. *IEEE Transactions on Electron Devices*, 48(3):552–9, 2001.

[4] B. P. Keller, S. Keller, D. Kapolnek, W. N. Jiang, Y. F. Wu, H. Masui, X. Wu, B. Heying, J. S. Speck, U. K. Mishra, and S. P. DenBaars. Metalorganic chemical vapor deposition growth of high optical quality and high mobility GaN. pages 1707–9, 1995.

[5] D. Kapolnek, X. H. Wu, B. Heying, S. Keller, B. P. Keller, S. P. DenBaars, and J. S. Speck. Structural evolution in epitaxial metalorganic chemical vapor deposition grown GaN films on sapphire. *Applied Physics Letters*, 67(11):1541–3, 1995.

[6] Amber Christine Abare. *Growth and fabrication of nitride-based distributed feedback laser diodes.* PhD thesis, University of California, Santa Barbara, 2000.

[7] B. P. Keller, S. Keller, D. Kapolnek, M. Kato, H. Masui, S. Imagi, U. K. Mishra, and S. P. DenBaars. Effect of atmospheric pressure MOCVD growth conditions on UV band-edge photoluminescence in GaN thin films. *Electronics Letters*, 31(13):1102–3, 1995.

[8] I. P. Smorchkova, C. R. Elsass, J. P. Ibbetson, R. Vetury, B. Heying, P. Fini, E. Haus, S. P. DenBaars, J. S. Speck, and U. K. Mishra. Polarization-induced charge and electron mobility in algan/gan heterostructures grown by plasma-assisted molecular-beam epitaxy. *Journal of Applied Physics*, 86(8):4520–6, 1999.

[9] I. P. Smorchkova, E. Haus, B. Heying, P. Kozodoy, P. Fini, J. P. Ibbetson, S. Keller, S. P. DenBaars, J. S. Speck, and U. K. Mishra. Mg doping of GaN layers grown by plasma-assisted molecular-beam epitaxy. *Applied Physics Letters*, 76(6):718–20, 2000.

[10] B. Heying, E. J. Tarsa, C. R. Elsass, P. Fini, S. P. DenBaars, and J. S. Speck. Dislocation mediated surface morphology of gan. *Journal of Applied Physics*, 85(9):6470–6, 1999.

[11] P. Kozodoy, Xing Huili, S. P. DenBaars, U. K. Mishra, A. Saxler, R. Perrin, S. Elhamri, and W. C. Mitchel. Heavy doping effects in Mg-doped GaN. *J. Appl. Phys. (USA)*, 87(4):1832–5, 2000.

[12] H. Katayama-Yoshida, T. Nishimatsu, T. Yamamoto, and N. Orita. Codoping in wide band-gap semiconductors. pages 747–56, 1999.

[13] J. S. Im, A. Moritz, F. Steuber, V. Harle, F. Scholz, and A. Hangleiter. Radiative carrier lifetime, momentum matrix element, and hole effective mass in GaN. *Appl. Phys. Lett. (USA)*, 70(5):631–3, 1997.

[14] Z. Z. Bandic, P. M. Bridger, E. C. Piquette, and T. C. McGill. Electron diffusion length and lifetime in p-type GaN. *Applied Physics Letters*, 73(22):3276–8, 1998.

[15] L. Chernyak, A. Osinsky, V. Fuflyigin, and E. F. Schubert. Electron beam-induced increase of electron diffusion length in p-type GaN and AlGaN/GaN superlattices. *Applied Physics Letters*, 77(6):875–7, 2000.

[16] J. C. Gonzalez, K. L. Bunker, and P. E. Russell. Minority-carrier diffusion length in a GaN-based light-emitting diode. *Applied Physics Letters*, 79(10):1567–9, 2001.

[17] S. Nakamura, T. Mukai, M. Senoh, and N. Iwasa. Thermal annealing effects on p-type Mg-doped GaN films. *Japanese Journal of Applied Physics, Part 2 (Letters)*, 31(2B):L139–42, 1992.

[18] James H. Edgar and INSPEC (Information service). *Properties of group III nitrides*. EMIS datareviews series ; no. 11. INSPEC Institution of Electrical Engineers, London, 1994.

[19] F. Bernardini, V. Fiorentini, and D. Vanderbilt. Spontaneous polarization and piezoelectric constants of III-V nitrides. *Physical Review B (Condensed Matter)*, 56(16):R10024–7, 1997.

[20] A. F. Wright. Elastic properties of zinc-blende and wurtzite AlN, GaN, and InN. *Journal of Applied Physics*, 82(6):2833–9, 1997.

[21] William Liu. *Handbook of III-V heterojunction bipolar transistors*. Wiley, New York, 1998.

3

Highly resistive base layer: The distributed device

3.1 Introduction

HETEROJUNCTION bipolar transistors in the III-N material system present a set of processing and material challenges distinct both from HBTs in other material systems and other devices in the III-N material system. The Mg doped base of the npn transistor currently causes the most difficulty. The base layer suffers from low conductivity, low minority carrier lifetimes, and contacts with a high sensitivity to etch damage and surface contamination. Because all conventional transistors have finite base conductivity, minority carrier lifetimes, and contact resistances, many of the issues related to the GaN:Mg base layer are extensions of common issues. Some of the effects that were obvious or even dominant in the AlGaN/GaN HBT are often negligible in conventional HBTs, however, and are therefore rarely mentioned. The parasitic collector current offset voltage in the common emitter mode is an example of one such effect. Initial results with the AlGaN/GaN HBT showed an offset voltage much higher than was expected. This chapter introduces those initial results, and discusses the analysis of the excess offset voltage as a "distributed device" effect. This is an effect which is due to the large voltage drops between the base contact and the base emitter junction in the AlGaN/GaN HBT. Finally, methods to reduce this offset voltage are presented. In later chapters, this conceptual framework will be used again with regards to the small signal RF performance (Chapter 6) and collector-emitter leakage currents(Chapter 5).

3.2 Initial Results

3.2.1 First demonstration of an AlGaN/GaN HBT

In May, 1998, UCSB demonstrated the first GaN based bipolar transistor[1]. Figure 3.1 shows the common emitter mode output characteristics of the device. The emitter finger was 1μm$\times$ 20 μm. The emitter contact was used as a mask for the emitter mesa etch, and additional base material was re-grown to bury the damaged base surface and reduce extrinsic base resistance as described in § 3.4.2. The entire layer structure for these devices was grown by MOCVD on C-plane sapphire. An n-type (Si doped) subcollector is followed by an unintentionally doped (UID) n-type GaN collector, a p-type (Mg doped) GaN base, and an n-type (Si doped) $Al_{0.1}GaN$ emitter (See Figure 3.1). The 500 nm emitter was doped 5×10^{18}cm^{-3} while the base layer

Output characteristics of the first AlGaN/GaN HBT

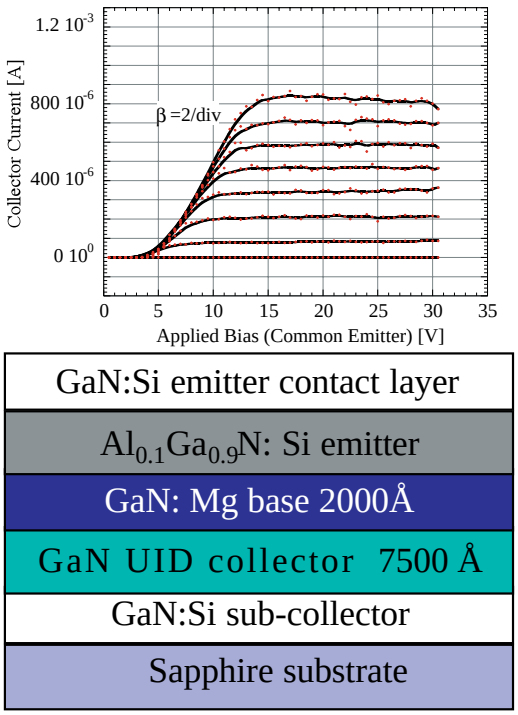

Figure 3.1: **Above:** Common emitter output characteristics of the first AlGaN/GaN HBT. The emitter is 1 $\times$ 20 μm. Base current steps are 50 μA.
Below: Layer structure for the device. Heterojunctions were graded. Base majority carrier concentration was$\sim1\times10^{18}$ cm^{-3} and emitter carrier concentration was $\sim5\times10^{18}$cm^{-3}.

was 200 nm of Mg doped GaN with an acceptor concentration of 1×10^{19}cm^{-3}. As explained in § 2.3.2, the incomplete ionization resulted in an expected carrier density of 8×10^{17}cm^{-3}. The resistivity of p-type material grown under similar conditions was 1.5 $\Omega\cdot$ cm resulting in sheet resistivities of 75 k$\Omega/\square$ for a 200 nm base. The background donor concentration in the collector is on the order of 5×10^{16}cm^{-3}. After growth, a tungsten emitter contact was deposited and subsequently used as a mask for the Cl_2 RIE emitter mesa etch (Figure 3.2). As discussed in § 3.4.2, base regrowth was used to bury surface damage caused by the emitter etch. Base contacts were deposited on the regrown mate-

Illustration of the AlGaN/GaN HBT

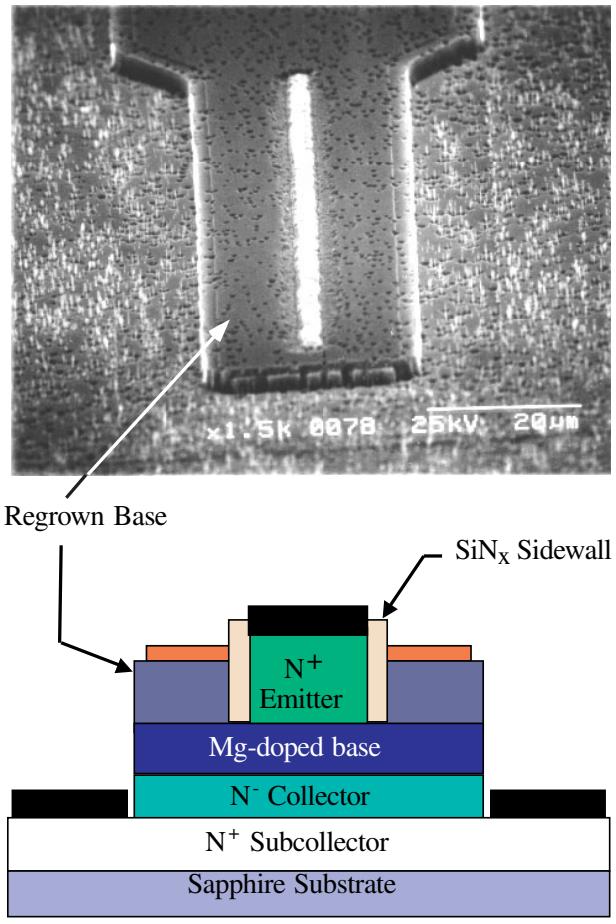

Figure 3.2: Cross-section and SEM image of completed device.

rial and the top of the SiN cap was removed to expose the emitter contact.

3.3 Electrical Characterization

An HP 4145 semiconductor analyzer and a Tektronix 370A curve tracer were used to perform the electrical characterization of these devices which were measured in the common emitter configuration. Gummel plots were also taken and are shown with V_{CB} = 0. Common emitter characteristics of a 1μm×20μm device (Figure 3.1) as well as a Gummel plot on a 20μm×20μm device (Figure 3.3) indicate a current gain (I_C/I_B) of 3.

3.3.1 Initial analysis

Aspects of the initial results presented above were unexpected. The collector current offset voltage in the common emitter characteristic and the low current gain in the Gummel characteristics were the most prominent. Analysis suggested that the high bulk base resistance and high contact voltage drop were responsible. The current gain is further discussed in Chapter 4.

Gummel plot of first AlGaN/GaN HBT

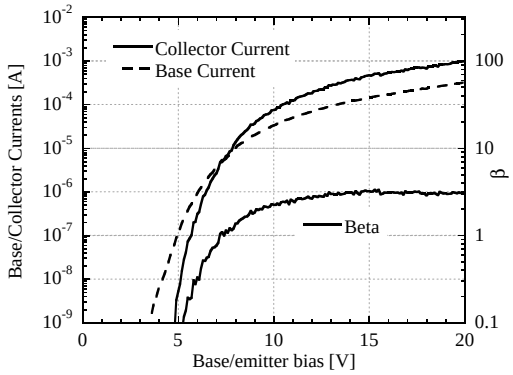

Figure 3.3: Gummel Plot of 20μm×20μmHBT with V_{CB}=0

Collector current offset voltage

The offset voltage is the collector-emitter voltage in the common emitter mode where the net collector current becomes positive. At this point, both the base-emitter and base-collector diodes are forward biased. From a simplified derivation of the Ebbers Moll model for a conventional graded HBT, the offset voltage, V_{OS}, can be written as[2]:

$$V_{OS} = \eta_C V_T \log\left(\frac{1}{\alpha_R}\right) + I_B R_E \qquad (3.3.1)$$

where η_C is the base-collector junction ideality factor, V_T is the thermal voltage, $\alpha_R \approx 0.1$ is the reverse current transfer ratio, and I_B and R_E are the base current and emitter resistance respectively. This expression was derived from the generalized drift-diffusion relations for the respective junctions, and predicts an offset voltage for the intrinsic device of much less than 1 V for low currents, while the offset voltages observed in the AlGaN/GaN HBT were in excess of 5V. Also, the offset voltages varied widely from device to device, which is inconsistent with the dependencies predicted by Eq. 3.3.1. The results indicated a parasitic offset voltage in addition to the ideal offset expected. It was observed that the turn-on voltage of the base contact was related to the offset voltage. The base voltage above the expected 3.4 V (intrinsic built in voltage) required to turn on the base emitter matched the excess offset voltage for the transistor. Figure 3.4 shows the high voltage barrier in the base contact and the resulting increase in the turn-on voltage of the base-emitter junction.

Base contact and emitter diode characteristics

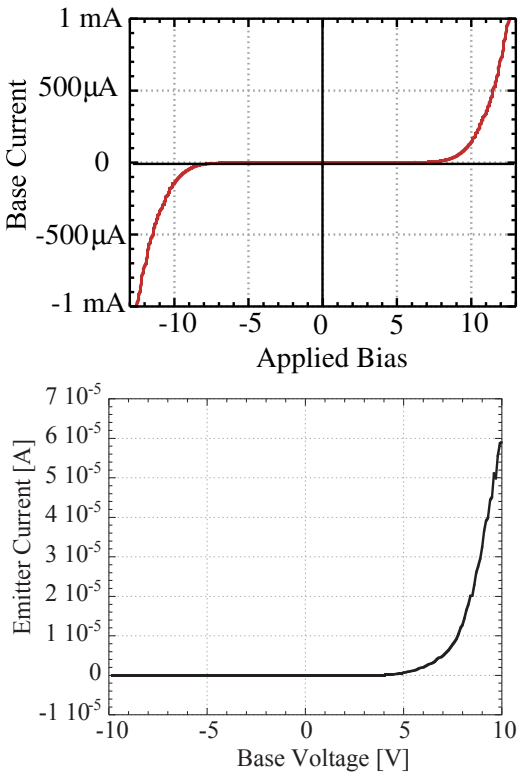

Figure 3.4: **Above:** Back to back base contacts show the nonlinearity in the base contact characteristics and the large voltage drop.
Below: Forward base emitter diode characteristic showing the increase in V_{BE} associated with the high base contact resistance and bulk sheet resistance.

Contact diagram

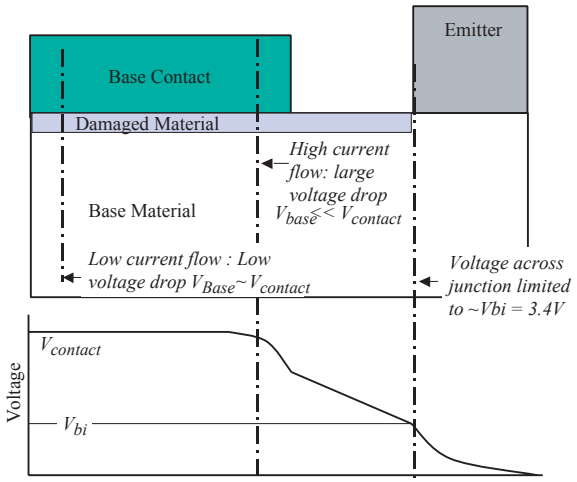

Figure 3.5: **Above:** This illustration shows the effect of the high contact resistance in the voltages near the base contact when the device is in the forward active mode. **Below:** This illustration represents the voltage gradients along the cross-section of the device due to contact and bulk resistances of the base layer.

In the ideal case, the base-collector bias is constant throughout the device. The voltage of the contact in the AlGaN/GaN HBT was substantially higher than the voltage of the base side of the emitter-base junction, however, because of the high lateral resistance and large voltage drop across the base contact. Figure 3.5 illustrates the potential drops in a device with high contact and sheet resistances. Also, because the contact characteristic is nonlinear, the voltage drop across the contact varies strongly with current density. This leads to a much larger voltage drop across the portion of the contact contributing to the lateral current which feeds the active transistor. Due to a much reduced current density, the base material at the outside perimeter of the base contact was not subject to this large voltage drop. This effectively divides the area under the emitter and the area under the majority of the base contact into two devices - the active transistor and a parasitic base-collector diode. The difference between the base voltage under the base contact and the base voltage under the emitter mesa at any given base injection current was the parasitic offset voltage of the transistor. A model was developed which accounted for the excess offset voltage by allowing for the difference in the bias condition of junctions in the intrinsic transistor and the base-collector junction outside the active device. The following example, illustrated by Figure 3.6 describes this model.

In this case the AlGaN/GaN transistor required a 6V base emitter contact voltage to inject a 100 μA base current, while the base-emitter junction forward bias required was only$\sim$3V. Because the base voltage under the extrinsic base contact is $\approx$ 6V, the collector-emitter voltage must be 3V for the extrinsic base-collector diode to have the same bias condition as the base-emitter junction. At lower collector-emitter bias, the base-collector diode under the base contact is forward biased even while the base-collector junction under the emitter mesa is zero-biased (Figure 3.6). The following are junction drift-diffusion equations for the collector current components in an HBT relevant to the common emitter offset voltage:

$$\mathbf{V}_{\text{offset}} \equiv \mathbf{V}_{CE}\Big|_{I_C=0} \qquad (I)(3.3.2)$$

$$I_{C_{\text{total}}} = I_{CE} - I_{BC_{\text{i}}} - I_{BC_{\text{x}}} \qquad (II)(3.3.3)$$

$$I_{CE} = \alpha \cdot A_{\text{emitter}} \cdot J_{s\ BE} \cdot \exp\left[\frac{V_{BE}}{\eta_E V_T}\right] \qquad (III)(3.3.4)$$

If $V_{CB_{\text{intrinsic}}} \neq V_{CB_{\text{extrinsic}}}$

$$I_{BC_{\text{i}}} = A_{\text{intrinsic}} \cdot J_{s\ BC} \cdot \exp\left[\frac{V_{BC_{\text{i}}}}{\eta_C V_T}\right] \qquad (IV)(3.3.5)$$

Offset voltage illustration

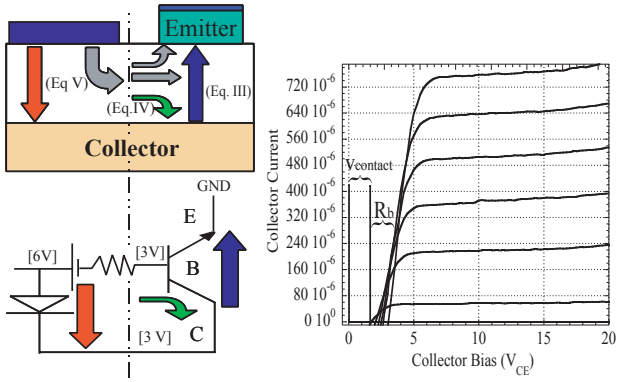

Figure 3.6: Large parasitic offset is due to the voltage drop associated with lateral base current. The numbered arrows in the schematic (above left) refer to equations which describe them. The voltages in the circuit diagram (below left) are examples of a bias condition in which the parasitic base-collector diode is forward biased, while the intrinsic device is zero-biased.

$$I_{BC_x} = A_{\text{extrinsic}} \cdot J_{s\ BC} \cdot \exp\left[\frac{V_{BC_x}}{\eta_C V_T}\right] \qquad (V)(3.3.6)$$

The roman numerals (I-V) correspond to the current paths shown in Figure 3.6. In the above equation α is an overall efficiency term that includes emitter injection efficiency as well as the transport efficiency across the base. Equations (IV) and (V) split from a single equation when the external base-collector bias differs from the internal bias. In this case, a higher collector contact voltage is required to turn off the extrinsic base collector diode. Figure 3.6 shows the contributions of the offset voltage equations to the total collector current, I_C. Analysis of a measured common emitter characteristic (Figure 3.6) show these effects on the DC performance. To reduce this offset voltage, the base contact and lateral resistances must be reduced- or the extrinsic base-collector junction eliminated. It is clear from the device characteristics in Figure 3.6 that this latter device exhibits a lower offset voltage than the initial device (Figure 3.1). The offset voltage has been reduced from 5V to 2.5V, and the knee voltage has been reduced from 15V to 6V. This improvement in output characteristics is substantially due to the process improvements described below.

3.4 Reducing the collector offset voltage through improved processing

In the course of the experiments on AlGaN/GaN HBTs, Both the regrown extrinsic base and the reduced damage emitter mesa etch process were developed to reduce the resistance in the base.

HBT with reduced offset voltage

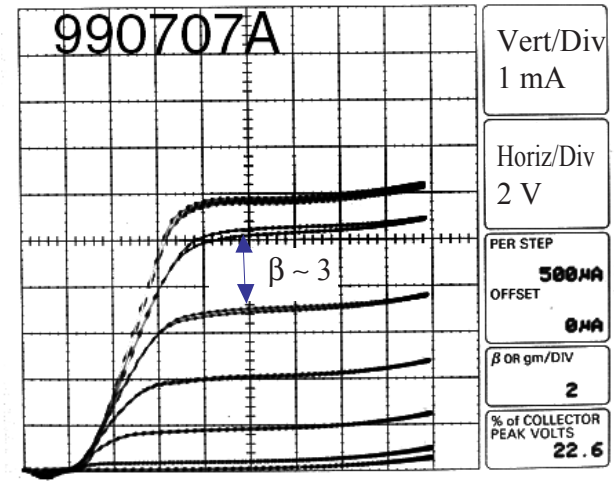

Figure 3.7: These output characteristics show a reduction of the offset voltages from previous devices. Although the layer structure is similar, the device active layers were grown by MBE instead of MOCVD, and devices were processed with improved methods aimed at reducing the offset and knee voltages.

3.4.1 Reducing the damage from the emitter mesa etch

An area of particular difficulty in the fabrication of the AlGaN/GaN HBT was the first step, the emitter mesa etch. Initially (when active layers were grown by MOCVD) material nonuniformity was a significant problem for etching the emitter mesa without also etching through the base layers. The implementation of the MBE grown active layers effectively solved this problem. The second major issue with the emitter mesa etch was the damage that was caused to the base layer. It was assumed that this damage could be reduced by reducing the power in the Cl_2 RIE etch. This assumption was confirmed by Kozodoy et al. [3] where the p-type contact quality was investigated for various chemistries and DC etch biases. The obvious solution of minimizing the emitter etch DC bias was complicated, however, by the vanishing etch rate of the AlGaN emitter at lower powers . It was believed that this slow etch rate of Al bearing layers was caused in part by oxidation of the surface. To deal with this complication, and increase the repeatability of the etch, a cleaning cycle was used to pre-condition the chamber, as well as an etch recipe that used short higher power bursts followed by a low power etch. To insure the cleanest possible etch, SiO_2 was used as an etch mask for the emitter etch. This also provided necessary contrast for alignments of future layers to the shallow etched emitter mesa, and was left on the emitter mesa until emitter contacts were applied, further protecting the surface during

Regrown extrinsic base HBT

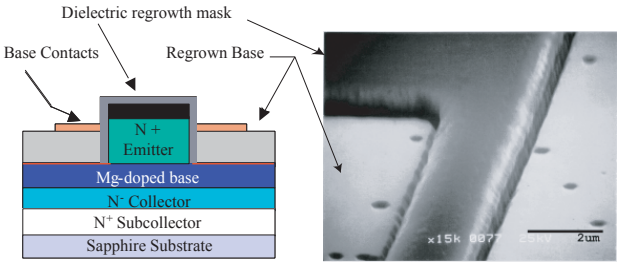

Figure 3.8: A reactively sputtered SiN_x cap is used as a regrowth mask for the selective area regrowth of 100 nm of Mg doped ($p \approx 1\times10^{18}$) contact layer. After regrowth, the SiN_x cap was removed and the standard process flow resumed.

Contact Comparison

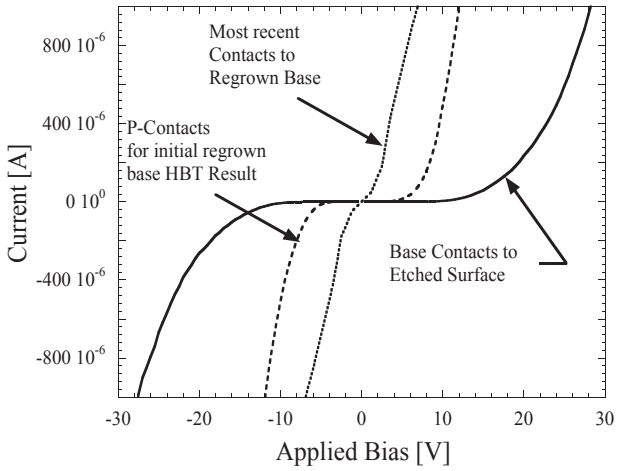

Figure 3.9: Comparison showing the I-V curve of adjacent p contacts on the 'as-etched' surface, contacts to the regrown surface, and finally, contacts to the regrown surface after an optimized etch

base contact processing. Figure 3.7 shows the improvement in device performance attained by changing to MBE grown active layers and using an optimized etch recipe.

3.4.2 Regrown Base HBT

Before the initial AlGaN GaN HBTs were successful, results showed extremely high base contact resistances. Voltages as high as 20V were required to turn on the base/emitter diode. The high voltage drop led to destructive heating of the base contact pads. To address the problem of high base contact resistance and reduce lateral access resistance in the highly resistive extrinsic base layer, the extrinsic regrown base process was developed. Figure 3.8 is an illustration of the cross section of the device with the regrown base layer added, as well as a Scanning Electron Microscope (SEM) micrograph of the regrown material surface.

The regrown extrinsic base process used a SiN_x cap to mask the emitter mesa. The wafer was then placed back in the growth chamber, and additional GaN:Mg material is grown. Because the GaN did not incorporate on the masked areas, the regrowth was selective and only occurred in the field. Typically, 100 nm of GaN:Mg with N_A=1×10^{19} cm^{-3} was grown for these devices. Next, the SiN_X cap was removed in concentrated HF. Because the extrinsic base layer is grown in an H_2 ambient, the Mg dopants needed to be thermally activated again (as described in § 2.5.1). Subsequent process steps including base metalization, base mesa etch and emitter and collector metalization were performed as outlined in § 2.5.4.

This process improved the performance of the devices sufficiently to allow for the devices to be operational in the common emitter configuration. The final version of this process substituted reactively sputtered AlN_x for the original SiN_x regrowth mask to avoid possible Si doping of the regrown material and add selectivity to AlGaN growth. . Figure 3.9 shows the improvements in contact quality achieved with first the regrown base process, and then further with the improved etched process described above. Although the regrown base process improved device performance by reducing the offset and knee voltages, it required several extra steps and was yield limiting. With the reduction of base surface damage associated with the emitter mesa etch improvement, the regrown base process became unnecessary, and was discontinued.

3.5 summary

Although initial results showed promise for continued improvement, the current gain was low, and a high collector offset voltage was attributed to high base resistance and a voltage barrier at the etch-damaged surface under the base contact. Originally, the high base resistance of these devices was expected to only effect the RF performance of the devices in combination with the parasitic capacitances of the device. The collector offset voltage was the first of the many DC and RF device characteristics to be unexpectedly dominated by the large voltage drop between the base contact and the base-emitter junction.

References

[1] L. S. McCarthy, P. Kozodoy, M. Rodwell, S. DenBaars, and U. K. Mishra. First demonstration of an algan/gan heterojunction bipolar transistor. pages 279–84, 1998.

[2] William Liu. *Handbook of III-V heterojunction bipolar transistors*. Wiley, New York, 1998.

[3] Peter Kozodoy. *Magnesium-doped gallium nitride for electronic and optoelectronic device applications*. PhD thesis.

4 Current gain

4.1 Introduction

In addition to the high collector current offset voltage, the DC output characteristics from Chapter 3 displayed low current gains. This chapter is focused on the common emitter current gain of the AlGaN/GaN HBT. For well designed conventional HBTs, the current gain can be predicted through simplified versions of the general relationships describing current flow in the transistor as a function of design and material variables. These approximations which are sufficiently accurate for conventional material systems are questionable for the AlGaN/GaN HBT.

The AlGaN/GaN HBTs presented here had current gains between 0.5 and 3.5. With such low gain in an HBT, recombination is likely to have played an important role. In the first half of this chapter, the dominant mechanisms relating to current gain and recombination in conventional HBTs are presented. First, in §4.2.1, the emitter injection efficiency describes the ratio electrons injected into the base to the back injection current of holes into the emitter. Secondly, in §4.2.2, the base current associated with electron-hole recombination in the space charge region is discussed, and finally, in §4.2.3, the base current associated with bulk recombination in the neutral base is presented.

In the second half of the chapter, results from experiments aimed at increasing the current gain in the device are discussed. The main thrust of this effort was directed towards reducing recombination in the bulk base layer. This was due to the already high injection efficiency as discussed in §4.3.2, and the difficulty in addressing the space charge recombination mechanisms. Design changes such as base thickness (§4.3.4), and base bandgap grading (§4.3.5) were expected to reduce the transit time across the base. Design and fabrication changes, however, where not expected to be successful in increasing carrier lifetimes either in the neutral base or the space-charge region of the base-emitter junction.

4.1.1 The ideal HBT: assumptions, and fundamental relationships

The gain element of a bipolar transistor is the forward biased base-emitter junction. The net gain is the electron current collected in the collector contact divided by the base current (I_C/I_B). The gain can be limited by the ratio of electron to hole current in the emitter-base junction and recombination in the junction and in the neutral base or sidewalls. Unless otherwise noted, these assumptions will be made for the following discussions:

Illustration of junction geometry terms

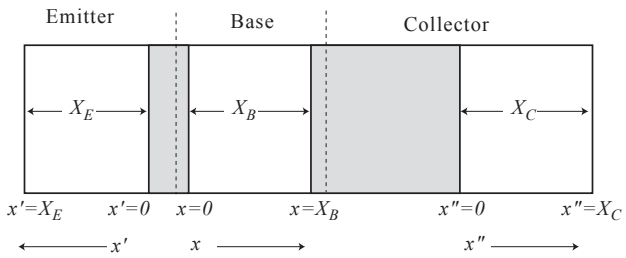

Figure 4.1: The naming conventions used to refer to various device parameters are listed above. The gray areas represent depletion regions of the junctions, while the white areas are the neutral base, emitter, and collector.

1. The abrupt depletion region approximation applies
2. The Maxwell-Boltzman approximation applies
3. The junction is under low injection conditions
4. Hole and electron currents are continuous

Although these assumptions may not always be true in these devices, the concepts remain pertinent. In the following sections, the base-emitter junction is assumed to be an $Al_{0.1}$GaN:Si/GaN:Mg graded N-p+ heterojunction. Figure 4.1 shows the coordinate system used for structural dimensions in equations relating to junction currents. The width of the neutral base and emitter are X_B and X_E respectively. Equilibrium electron and hole concentrations are n_{E_0}, p_{E_0} in the emitter, and n_{B_0}, p_{B_0} in the base. Each neutral region has a positive coordinate system radiating from the depletion region edge, with $0 < x' < X_E$ in the neutral emitter, and $0 < x < X_B$ in the neutral base.

4.2 Theory of current gain in the HBT

Figure 4.2 displays the sinks for base current in an idealized HBT. These current sinks correspond to the loss mechanisms in the current gain.

Dominant base currents in a conventional HBT

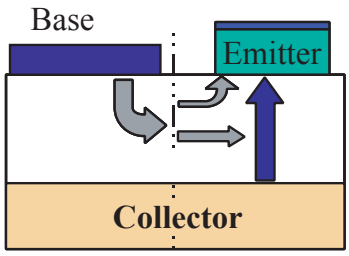

Figure 4.2: Illustration of currents in an idealized vertical bipolar transistor. Base currents are required to support the base emitter junction in the form of recombination and emitter injection as well as supporting the bulk base for bulk recombination of minority electrons. Reverse injection from the base-collector junction is neglected.

The complimentary form of the common emitter current gain, the common base current gain, α, provides a convenient form for understanding the effects of the current sinks on the current gain. These figures of merit are related as: $\alpha \equiv (1/\beta + 1)^{-1}$. Where α is always less than 1, and can be expressed as a product of several elements:

$$\alpha = \gamma_i \, \delta \, \alpha_T \tag{4.2.1}$$

Here γ_i, δ, and α_T are the emitter injection efficiency, the base-emitter recombination factor, and the transport factor respectively. These elements are explained below.

4.2.1 Emitter injection efficiency in the HBT

Because the emitter injection efficiency in a graded heterojunction HBT depends only on the minority carrier ratio and layer thickness of the base and emitter, it was expected to behave according to theory. Based on a derivation by William Liu in *Handbook of III-V Heterojunction Bipolar Transistors*[1], for the case where $L_B \gg X_B$ and $L_E \gg X_E$, the emitter injection efficiency is:

$$\gamma_i = \left(1 + \frac{p_B \, \mu_E^h \, X_B}{n_E \, \mu_B^e \, X_E} \cdot \exp\left[-\frac{\Delta E_g}{kT}\right]\right)^{-1} \tag{4.2.2}$$

It is clear from Eqn.4.2.2 that both the bandgap and doping concentration will effect the injection efficiency. The ratio of minority carrier mobilities, (μ_E^h/μ_B^e), refers to the hole and electron mobilities in the emitter and base respectively, and is expected to be less than 1 due to the high effective mass of holes in the III-N material system. Although the base acceptor concentration is much larger than the emitter donor concentration, due to the partial ionization of the acceptors in the base, the hole concentration in the base, p_B is typically less than the electron concentration in the emitter (n_E). The exponential dependence on the change in bandgap, ΔE_g, is due to the effect it has on the minority carrier concentration. As explained in § 2.4.1, the change in bandgap for Al GaN is expected to be $\sim 10kT$. In this case, the exponential dominates the other terms which are all expected to be less than 1. For this reason, in the HBT, the injection efficiency is expected to be near unity.

Injection efficiency for BJT and HBT

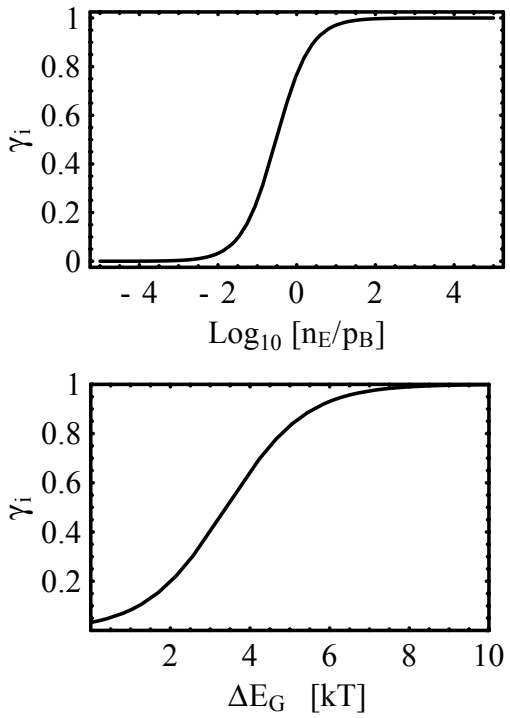

Figure 4.3: Injection efficiency Calculated using Eqn. 4.2.2, assuming $\mu_{h_E} = 30\,\mathrm{cm}^2(\mathrm{V}\cdot\mathrm{s})^{-1}$, $\mu_{e_B} = 100\,\mathrm{cm}^2(\mathrm{V}\cdot\mathrm{s})^{-1}$, and $X_E = X_B$.
Above: Injection efficiency as a function of base-emitter doping ratio for homojunction
Below: Injection efficiency as a function of base-emitter bandgap change, assuming $p_{0_B}/n_{0_E} = 100$.

4.2.2 Recombination in the emitter-base junction

Carrier recombination in the space charge region of the base-emitter junction is a function of the trap densities in the region, and was expected to be significant in GaN bipolar transistors. Still, little is known about the specifics of carrier lifetimes and trapping mechanisms in the base-emitter junction. For this reason the calculations used here are simplified and illustrate the effect with examples using estimated values.

The recombination factor, δ, can be estimated using the Shockley-Read-Hall relations for recombination assisted by impurity or trap states. For a forward biased junction, the recombi-

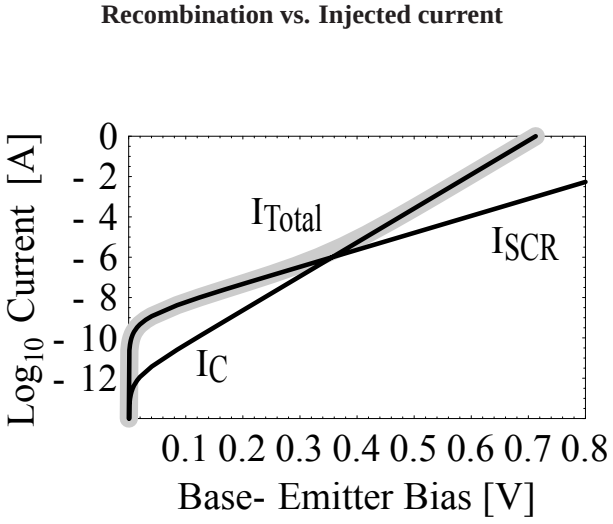

Figure 4.4: Illustration of calculated currents for recombination or injection. Ideal diode equation was used to illustrate the total current in a system when the recombination current coefficient is higher than the reverse saturation current. I_{SCR} follows Eq. 4.2.3, with an ideality factor of 2, while the I_C curve has an ideality of 1.

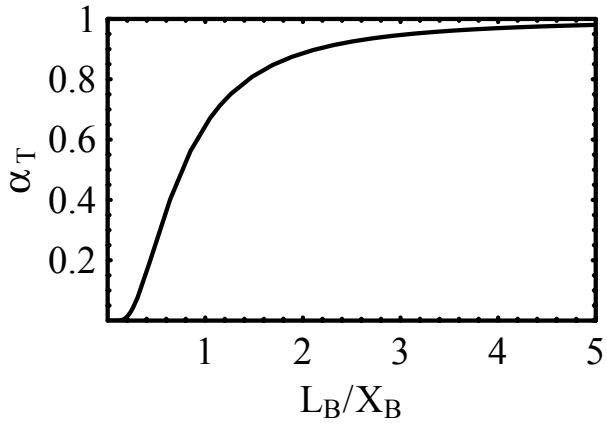

Figure 4.5: Dependence of α_T from Eq. 4.2.5.
Transport factor as a function of the ratio of X_B to L_B.

nation current density, J_{rec} in a conventional HBT can be written as:

$$J_{rec} = J_{r0}\left(\exp\left[\frac{qV_{be}}{\eta kT}\right] - 1\right) \tag{4.2.3}$$

where J_{r0} is the equilibrium recombination current and dependent upon material properties which for GaN are not well known. The 'η' in the denominator of the exponential is the ideality factor for this current mechanism. This unit-less value can vary between 1 and 2 depending on the specifics of the recombination current. The forward current, injected as minority carriers in the base, follows a relationship with V_{BE} of:

$$J_C = J_s\left(\exp\left[\frac{qV_{be}}{kT}\right] - 1\right) \tag{4.2.4}$$

Typically, however, J_{r0} is greater than J_s (the reverse saturation current), suggesting that at low currents the space charge recombination dominates the forward current of the diode as shown in Figure 4.4. As the forward voltage increases, however, the higher ideality factor of the recombination current allows the forward injection current to become dominant. Because the current that recombines in the base-emitter junction does not reach the collector, it represents a loss of current gain. The illustration in Figure 4.4 shows that for $J_{r_0} > J_s$, the current gain will be low until the cross-over point where the injection current dominates.

4.2.3 Base transport factor

As electrons injected at the edge of the base-emitter depletion region diffuse across the base of the transistor, some of the carriers recombine. This recombination is a sink for holes in the base, leading to a reduction of gain. The base transport factor, α_T, is the fraction of electrons that transit the base and are collected in reverse biased base-collector junction. In the forward active mode, the transport factor can be written:

$$\alpha_T = \frac{J_{nC}}{J_{nE}} \cong \frac{\exp\left(V_{BE}/V_T\right) + \cosh(X_B/L_B)}{1 + \exp\left(V_{BE}/V_T\right)\cosh(X_B/L_B)} \tag{4.2.5}$$

Figure 4.5 shows α_T as a function of the ratio of the diffusion length of electrons in the base to the length of the neutral base. It is clear that the dependence is strongest when the ratio is less than 1.5. For conventional transistors where the base width, X_B, is much less than the minority carrier diffusion length in the base, L_B, Equation 4.2.5 can be further approximated as:

$$\alpha_T \cong \frac{1}{\cosh\left(X_B/L_B\right)} \tag{4.2.6}$$

and taking the first two terms in the Taylor series expansion of the $\cosh$ term,

$$\alpha_T \approx \frac{1}{1 + \frac{1}{2}\left(X_B/L_B\right)^2} \approx 1 - \frac{1}{2}\left(X_B/L_B\right)^2 \tag{4.2.7}$$

An alternative expression for α_T is the ratio of the electron transit time across the base, τ_b and the electron lifetime in the base τ_n:

$$\alpha_T = \left(1 + \frac{\tau_b}{\tau_n}\right)^{-1} \tag{4.2.8}$$

Many of the methods for increasing the current gain of the device focus on reducing the base transit time as this also improves RF performance.

Calculated Gummel using ideal diode eqns.

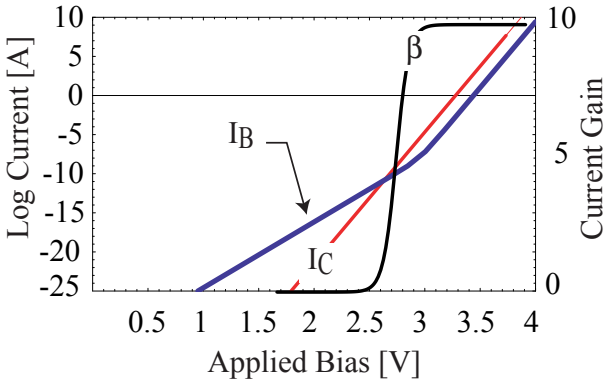

Figure 4.6: Plot of collector and base current using ideal diode equations, 4.2.3, 4.2.4, and Eqn.4.2.5. Base current dominates at low currents where the recombination current is larger than the injected current. As V_{BE} increases, the injected current begins to dominate.

4.2.4 Calculated current gain for AlGaN/GaN HBT

Combining the terms relating to current gain, the injection efficiency, the bulk recombination and space charge recombination (Eqn.4.2.2, 4.2.3, and Eqn.4.2.7) results in the overall current gain for the device. Figure 4.6 shows a calculated Gummel characteristic for such a device. Unfortunately, because the lifetime in the emitter-base junction is unknown, J_{r_0} was chosen arbitrarily for this calculation. The effect of the ratio of J_{r_0}/J_s, however, is to delay the onset of gain, and does not effect the gain at higher currents which is limited by the recombination in the bulk. From Bandic et al. [2], the electron diffusion length is taken to be 200 nm, μ_B^e was 200 $\text{cm}^2(\text{V}\cdot\text{s})^{-1}$. The device geometry was a fairly typical 1×50 μm, and the structure was typical of the devices fabricated with $X_B = 100$ nm, $n_E = 5{\times}10^{18}\text{cm}^{-3}$, $p_b = 1{\times}10^{18}\text{cm}^{-3}$.

This calculation did not make the short base approximation ($X_B \ll L_B$) but it does assume an absence of electric field in the base and neglects the reverse current of the collector-base junction. From Figure 4.6, it is clear that the current gain is less than one until the injected current has overcome the recombination current. The level of saturation of the current gain is a function of the recombination rate in the base. The recombination rate is incorporated through the value of L_B which was taken from the empirical data of another group [2], and may therefore differ from the material used for the devices. This calculation also neglects resistive elements in the base and emitter, so the V_{BE} shown in Figure 4.6 must be assumed to be the bias at the junction itself.

Initial results for AlGaN GaN HBT

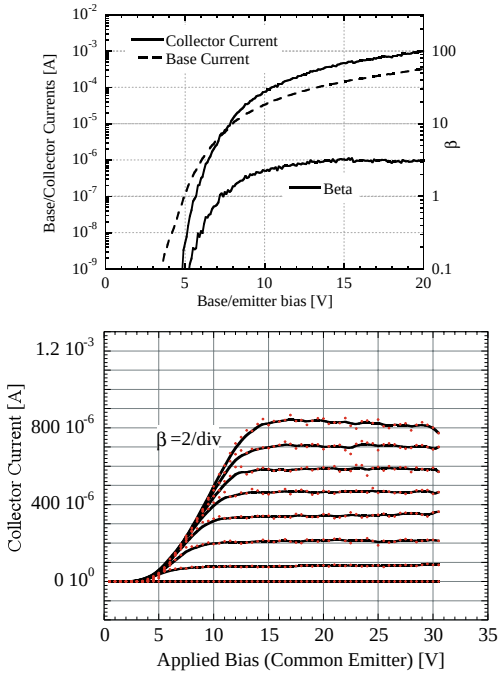

Figure 4.7: Gummel and output characteristics for the first AlGaN/GaN HBT.

4.3 Current gain measurements in the AlGaN/GaN HBT

4.3.1 Initial results

As discussed in Chapter 3, initial AlGaN/GaN HBTs had low current gains, $\beta \approx 3$. It was believed that the low current gain was due to high levels of recombination in the neutral base and in the forward biased base-emitter junction. Many of the material characteristics such as minority carrier lifetimes and depletion region recombination rates, however, were unknown. Also, due to the non-linear base contact current-voltage characteristic, and possibly other voltage drops in the device, the diode characteristics of the base emitter junction typically displayed ideality factors greater than 2. And, due to the high series resistance in the base, the junction current was quickly series resistance limited. For this reason, it was difficult to determine the source of the recombination. To improve the current gain of the devices, therefore, an empirical strategy was adopted. First, the injection efficiency component of current gain was investigated.

4.3.2 Current gain in HBT vs BJT

From Eqn.4.2.2 (See Figure 4.3), the injection efficiency even in a BJT was expected to be greater than 90%. Due to the high

Effect of heterojunction on current gain

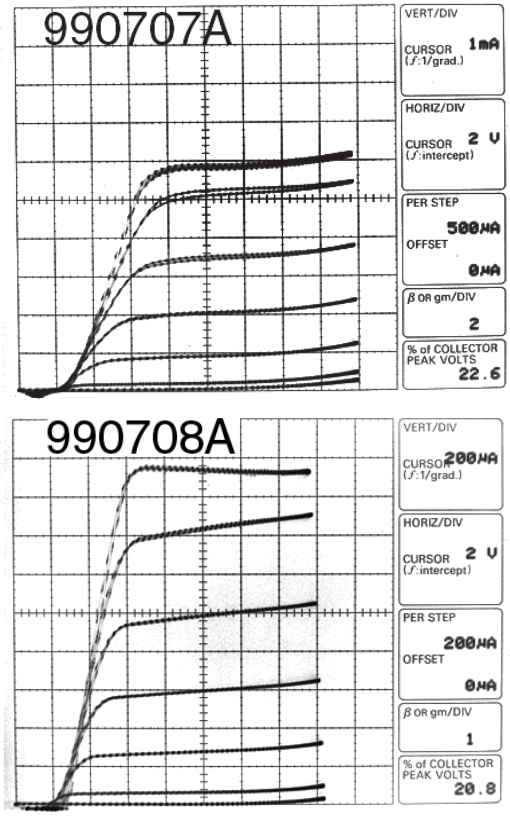

Figure 4.8:
Above: Common emitter characteristics of an MBE grown HBT. $\beta \cong 3$
Below: Common emitter characteristics of an MBE grown BJT grown on the same template and processed in parallel.$\beta \cong 2$

2-D Simulations projecting improved current gain with bandgap engineering and base width design

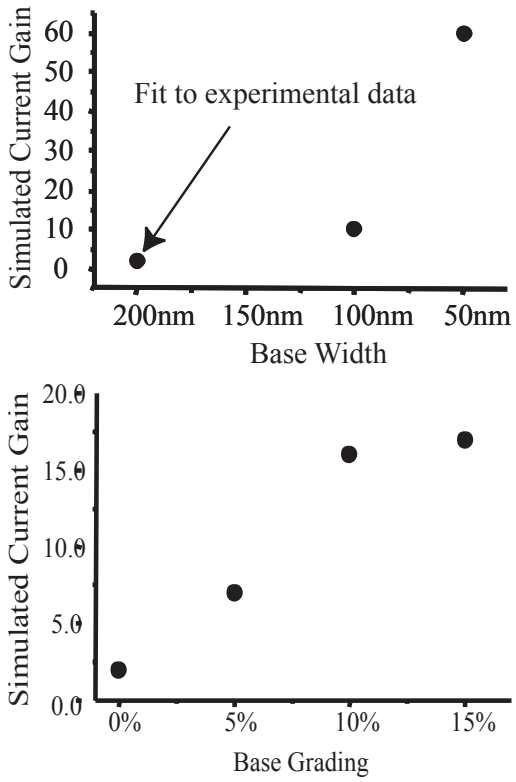

Figure 4.9: Two dimensional simulations of the AlGaN/GaN HBT structure.
Above: Projected current gain as a function of base width.
Below: Projected current gain as a function of base compositional grade (inducing quasi-electric fields)

activation energy of Mg in the base, the carrier concentration was likely to be an order of magnitude lower in the base than in the emitter. Also, because of the high effective mass, the hole mobility in the emitter was expected to be smaller than the electron mobility in the base. Figure 4.8 shows a comparison of a BJT and an HBT grown by MBE on consecutive days on the same MOCVD template and processed concurrently. Although slightly misleading because the characteristics were taken on a different current scale, the maximum current gain of the HBT is about 3, while the maximum current gain of the BJT is about 2. The result suggests that in these structures the injection efficiency was not limiting the current gain. For the HBT, the change in bandgap insures that the injection efficiency is near unity, therefore, it is likely that the product of the other factors, the base transport factor (α_T) and the base-emitter junction recombination factor, δ, is $\alpha_T \cdot \delta \approx 0.75$, corresponding to a gain of 3 with 100% injection efficiency. If nothing else was changed, the drop in gain in the BJT corresponds to a drop of injection efficiency of about 11% to 89%. Because the back injection of holes into the emitter has an inverse exponential dependence on bandgap difference between the base and emitter in the HBT, and in the BJT depends principally on the ratio of the doping concentrations, the injection efficiency was expected to be more repeatable and predictable than other the other factors in the HBT which depend more strongly on carrier lifetimes. There may also be interaction effects, however whereby the Al concentration in the emitter may effect, for example, the junction recombination factor, δ.

4.3.3 Current gain simulations for the AlGaN/GaN HBT

Two dimensional simulations were performed by Prof. David Pulfrey to predict the current gain of the HBT as a function of various design variables. We concentrated on the base thickness and bandgap grading in the base to evaluate the methods for reducing base transit time (τ_B). Figure 4.9 shows the simulated

Thin vs. Standard base width

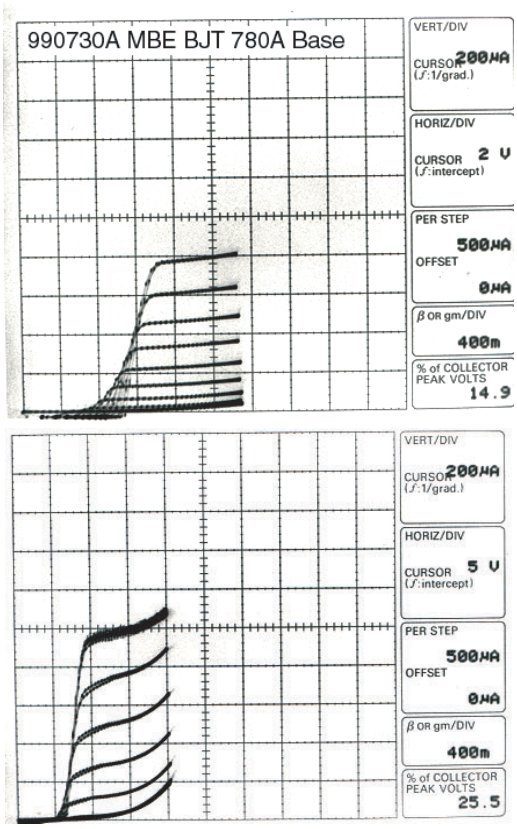

Figure 4.10: **Above:** BJT grown by MBE with a thinner (78 nm) base layer. **Below:** HBT grown by MBE with a standard base thickness of 100 nm.

Band diagram of HBT with energy gap grading in the base

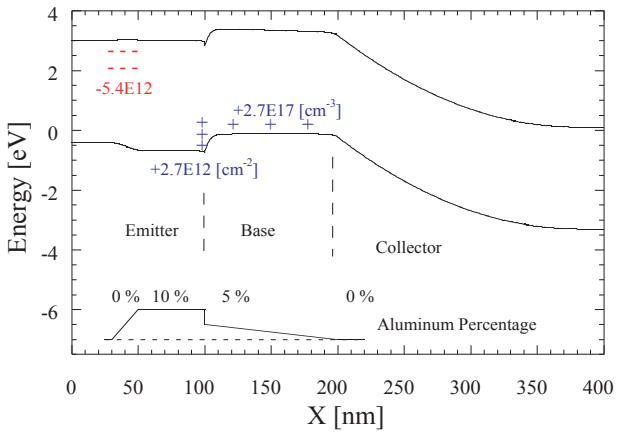

Figure 4.11: Illustration of a band diagram of an HBT with aluminum compositional grading in the base. The grading changes the bandgap, inducing quasi-electric fields, but also induces polarization charge. The slope in the conduction band was expected to reduce carrier transit time and thereby increase gain.

current gain of the HBT with a reduction of base thickness and increase in Al grading across the base. The first data point is a device with a structure similar to the HBTs shown in Figure 4.7. These simulations assume that the carrier lifetime in the base is a dominant factor. This is expected due to the high dopant concentration in the base which is expected to reduce the carrier mobility and increase recombination rates. Reports of minority carrier diffusion lengths in p-type GaN support this[2].

4.3.4 Reduced base width HBT

Simulations (Figure 4.9) showed a significant increase in current gain when the base width dropped below 100 nm. To test this prediction, devices were grown by MBE with varying base layer thickness. As mentioned earlier, the typical base thickness for devices grown by MBE was 100 nm. Figure 4.10 shows the result. Again, the two devices were grown on the same MOCVD template and processed concurrently. The BJT had a reduction in base thickness of 22%. Using Eqn.4.2.7 to approximate the change in current gain, we would expect to double the gain of the device. The low gain in this case of both the HBT and BJT, however, suggest that in this case the gain may be limited by the base-emitter junction recombination current, J_{SCR}. For example, a gain of 0.5 corresponds to $\alpha = 1/3$. For the HBT, if we assume 100% injection efficiency, the product of the recombination terms, $\alpha_T \delta$ is then 1/3. For the thin base BJT, if the junction recombination rate is unchanged and the injection efficiency is reduced to 89% for the BJT as discussed above, α_T is expected to increase by 25%. This would imply that α_T was 83% for the thin base BJT, and 66% for the thicker base HBT, with a recombination factor, δ of 50% for both. Of course, this example was based on the short bas assumption ($X_B \ll L_B$), among others, which, if invalid, may effect calculations.

4.3.5 Quasi-electric fields in the base: Bandgap grading

Although reducing the width of the neutral base reduces the transit time, it also increases the base resistance. Grading of the bandgap in the base, however, creates a quasi-electric field in the base. The quasi-electric field is a slope in the conduction band, and has the same effect as an electric field, but only on the carriers in the conduction band. The quasi-field adds a drift component to the base current, and thereby reduces the transit time of carriers in the base. Typically, this is used in high frequency devices to reduce the diffusion capacitance associated with the base transit time, but it also has the advantage of reducing recombination in the base.

This effect was studied in the AlGaN/GaN HBT for enhance-

Effect of base compositional grading on current gain

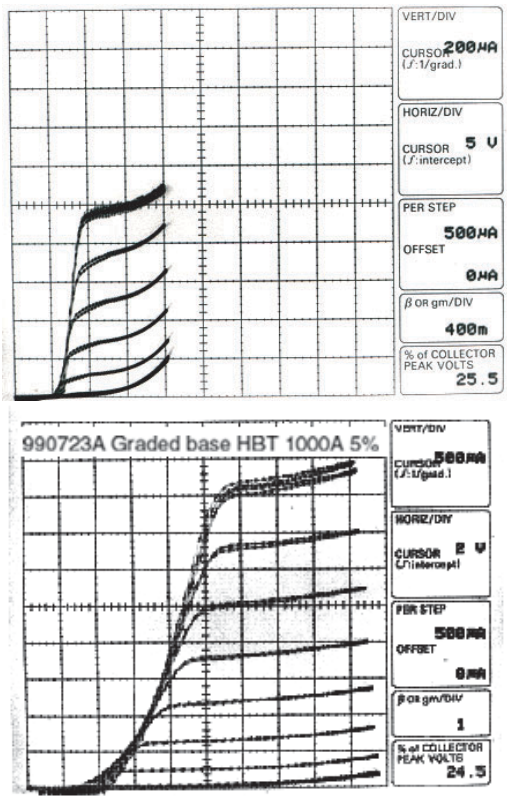

Figure 4.12: **Above:** Common emitter characteristics of an MBE grown HBT($\beta \cong 0.5$).
Below: Common emitter characteristics of an MBE grown HBT with a linear grade from 0-5% in aluminum composition across the base to induce quasi-electric fields ($\beta \cong 1.5$).

ment of the current gain. Devices were grown by MBE with a grade of aluminum percentage across the base from 0 at the collector junction to 5% at the emitter side of the base. Figure 4.9 shows the expected enhancement in current gain with grading percentage. This enhancement comes from a reduction in the base transit time, τ_b, which differs from the non-graded case, τ_{b_0} by $f(\kappa)$ (a factor proposed by Liu[1] to represent the enhancement due to a drift component in minority carrier current across the base) and can be expressed as:

$$\tau_b = \tau_{b_0} \cdot f(\kappa) \tag{4.3.1}$$

where

$$f(\kappa) = \frac{2}{\kappa}\left(1 - \frac{1}{\kappa} + \frac{1}{\kappa}\exp(-\kappa)\right) \tag{4.3.2}$$

and $\kappa = \Delta E_g/kT$. Figure 4.12 shows common emitter characteristics comparing two structures. The wafer with the graded aluminum composition in the base showed an increase of current gain from 0.5 to 1.5. The expected enhancement in current gain can be calculated from:

$$\beta = \frac{J_C}{J_p + J_{SCR} + J_{bulk}} \tag{4.3.3}$$

Where J_C, J_p, J_{SCR}, and J_{bulk} are the current densities relating to the collector , hole injection into the emitter, space charge region recombination, and base bulk recombination respectively. As discussed in §4.3.2, for the HBT we can assume that the injection efficiency, γ_i is near 1, and therefore J_p can be neglected. The quasi-field in the base adds the $f(\kappa)$ term from Eq. 4.3.2 giving:

$$\beta = \frac{J_C}{J_{SCR} + J_{bulk} f(\kappa)} \tag{4.3.4}$$

In this case, $f(\kappa) = 0.32$. We then have:

$$\frac{J_C}{J_{SCR} + J_{bulk}} = 0.5 \tag{4.3.5}$$

$$\frac{J_C}{J_{SCR} + J_{bulk} f(\kappa)} = 1.5 \tag{4.3.6}$$

Solving this system of equations, it is clear that for this case the bulk recombination dominates:

$$J_{bulk} = 50 J_{SCR} = 1.96 J_C \tag{4.3.7}$$

This result strongly contradicts the analysis of the thin base BJT, leading to the conclusion that both the bulk and base-emitter recombination rates may vary significantly from device to device and from wafer to wafer. To some extent, this may also be due to enhancement of sidewall recombination due to emitter crowding effects.

4.3.6 Emitter current crowding: Effective emitter area

Due to the high sheet resistance in the base, a significant lateral voltage gradient exists in the base in the forward active mode. Recalling from § 2.3.2 that the lateral resistance is on the order of 100 kΩ/□ in the 100 nm p-type base, it is clear that under forward bias, the lateral voltage drop in the base is significant. Figure 4.13 illustrates the effect of the base resistance on the emitter current density in the forward active mode. The base-emitter voltage as a function of x is then:

$$V_{BEj}(x) = V_{BEj}(0) - \int_0^x J_B(x')\rho_B dx' \tag{4.3.8}$$

Following the derivation from [1], the effective emitter width is defined as the emitter width that would result in the same current level, but assuming a uniform current density. The ratio of the effective emitter width to the actual emitter width, W_{eff}/W_E is then:

$$\frac{W_{eff}}{W_E} = \frac{2}{W_E J_E(0)} \int_0^{W_E/2} J_E(x)dx = \frac{\sin c \cos c}{c} \tag{4.3.9}$$

Illustration of emitter crowding effect

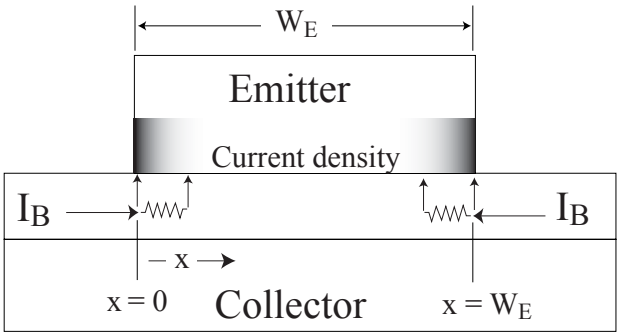

Figure 4.13: Illustration showing the emitter crowding effect in the AlGaN/GaN HBT. The majority of forward active current flows near the emitter mesa sidewall as shown.

where c is given by the transcendental equation:

$$c \tan c = \frac{q}{kT} \frac{I_E}{X_B} \frac{\rho_B}{4(\beta+1)} \frac{W_E}{L_E} \tag{4.3.10}$$

Where $J_E(0)$ is the apparent emitter current density and ρ_B is the base resistivity.

Figure 4.14 shows the effect of emitter current and base resistivity on the effective emitter area as calculated from Eqns. 4.3.9 and 4.3.10. For a device with a current gain of 3.5, a base resistivity of 1 Ω cm, and a thickness of 100 nm, the effective emitter width is ∼0.2μm when driven with a 1 mA emitter current across an emitter stripe 50 μm long.

The emitter crowding may effect the current gain of the device in two ways. First, the severe crowding results in a significant emitter area which is forward biased to a lesser degree than the edge. Because J_{SCR} dominates at low currents, this may result in a higher proportion of recombination in the space-charge region. Secondly, because the sidewalls of the device are unpassivated, the recombination current near the sidewall is expected to be higher than that in the bulk. Due to the severe current crowding, the majority of the current flow occurs at the edges of the device, and therefore may be subject to increased recombination. From Figure 4.14, it is also clear that the increase in current across the device increases the degree of crowding. Also, as the current crowds to the edge and the gain drops, the voltage drop in the base increases, further restricting the base current to the edge of the device. Because the effective width decreases with forward current, this may lead to an inverse relationship between forward current and β, resulting in a premature saturation of the current gain - as seems to be the case in the AlGaN/GaN HBT.

Effective emitter width vs emitter current and bulk resistivity

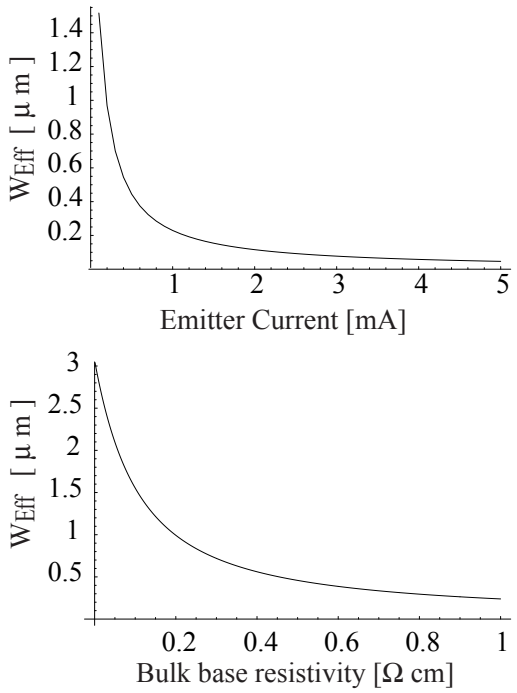

Figure 4.14: Calculated effective emitter width from Eqns.4.3.9 ,4.3.10 for a structure with β = 3.5, Ω·cm, X_B=100 nm, W_E = 3 μm, L_E = 50 μm.
Above: Effective emitter width as a function of emitter current ($\rho_B = 1\Omega \cdot cm$).
Below: Effective emitter width as a function of bulk resistivity in the base $I_E = 1mA$.

4.4 Summary

Basic relationships for the current gain elements, and recombination elements are presented, followed by experimental results of initial HBTs, and devices with design changes addressing the expected base current sinks in the device. Base-emitter injection efficiency is estimated to be high even in the case of the BJT (∼90%), and near unity for the HBT. Comparison of a BJT and HBT structure support this conclusion, suggesting that the cause for the low current gains observed is due to recombination either in the neutral base or in the base-emitter space charge region. Next, following the direction of device simulations, devices with a reduced base width and devices with a quasi-electric field introduced in the base with Al alloy grading were investigated. Although both examples showed some improvement, there was a contradiction in the results regarding the determination of the dominant recombination mechanism. Finally, emitter current crowding was introduced as a possible contributing factor to the low current gains, as it was expected to increase both

the junction and bulk recombination currents.

References

[1] William Liu. *Handbook of III-V heterojunction bipolar transistors*. Wiley, New York, 1998.

[2] Z. Z. Bandic, P. M. Bridger, E. C. Piquette, and T. C. McGill. Electron diffusion length and lifetime in p-type gan. *Applied Physics Letters*, 73(22):3276–8, 1998.

5

Emitter-collector leakage and dislocations in GaN HBTs

5.1 Introduction

MANY of the devices fabricated in the course of the studies presented in this dissertation suffered from higher than expected output conductance, and in severe cases, an emitter-collector short circuit. Also, initial reports of GaN HBTs from other groups often only provided common base characteristics or Gummel characteristics of devices[1], citing excessive collector leakage as the cause for a lack of common emitter operation. The effect of this leakage is discussed in §5.2.1

To understand these unexpected results, several experiments were performed on the effect of dislocation densities and doping on emitter-collector leakage. Previously, the effect of dislocations on reverse current in GaN p-n diodes had been reported by Kozodoy et al.[2]. Also, dislocations have been shown to have an important effect in optical devices including lasers[3] and avalanche photodiodes [4]. Because the threading dislocation densities in hetero-epitaxial GaN films tend to vary from one growth to another, it was determined that the preferred method to study the effect of dislocations was to fabricate devices on templates grown using the Lateral Epitaxial Overgrowth (LEO) technique. The growth, fabrication, and the results of device testing are discussed in §5.2.1, where it is seen that the emitter-collector leakage was reduced by several orders of magnitude on regions of reduced dislocation density.

To further understand the mechanism responsible for the emitter-collector leakage, an experiment was performed on samples with varying base doping (§5.4). It was found that an increase in base doping significantly reduced the emitter-collector leakage, suggesting that the leakage mechanism was a localized punch through effect surrounding the dislocation.

5.2 Emitter-collector leakage

The observed characteristics of the emitter-collector leakage varied widely from device to device and wafer to wafer, but a common element was a premature breakdown of the collector-emitter current-voltage characteristic. In the forward active mode the collector-base junction is reverse biased, and expected to have a high breakdown voltage. Figure 5.1 shows an MOCVD grown BJT with a breakdown voltage over 80V. Sometimes, however, devices with a similar structure showed much higher leakage. Figure 5.2 shows the common emitter characteristics of a device with much higher leakage at relatively low voltages, and the I-V curve of the collector-emitter leakage. In addition to a higher than expected output conductance, the emitter collector leakage can affect other aspects of the output characteristics of the device.

High voltage operation of AlGaN/GaN HBT

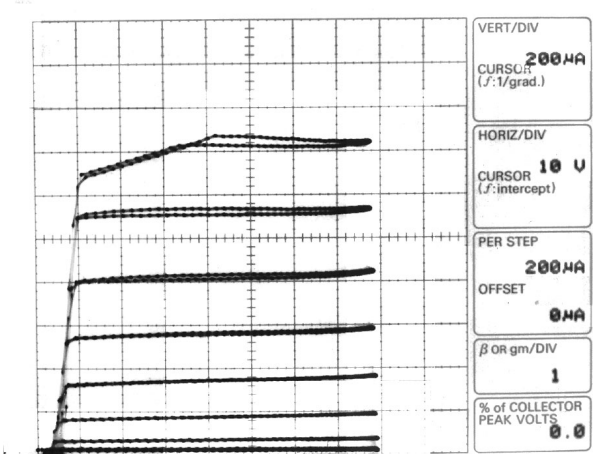

Figure 5.1: Common emitter characteristics of an AlGaN/GaN BJT showing operation over 80V. $\beta \sim 1$.

5.2.1 Effect of leakage on device characteristics

For devices with severe leakage, it was found that the current gain measured using common emitter characteristics and Gummel plots differed significantly. As described in Chapter 3 the high base contact resistance and lateral base resistance cause a disparity between the base voltage under the contact and under the emitter mesa. When combined with a collector-emitter leakage mechanism, this voltage disparity causes Gummel plots to be unreliable for the determination of current gain. For example, if the base-emitter *contact* voltage is 10V, and V_{CB} is set at zero, the actual collector-base voltage under the emitter mesa is 7V reverse, and the collector-emitter voltage is 10V. In devices that suffer from collector-emitter leakage, the forward current resulting from leakage may be greater than the current associated with the transistor action of the device. In this situation, the transistor current cannot be distinguished from the leakage current. A Gummel plot of a device with leakage current is shown

Collector-emitter leakage in an HBT

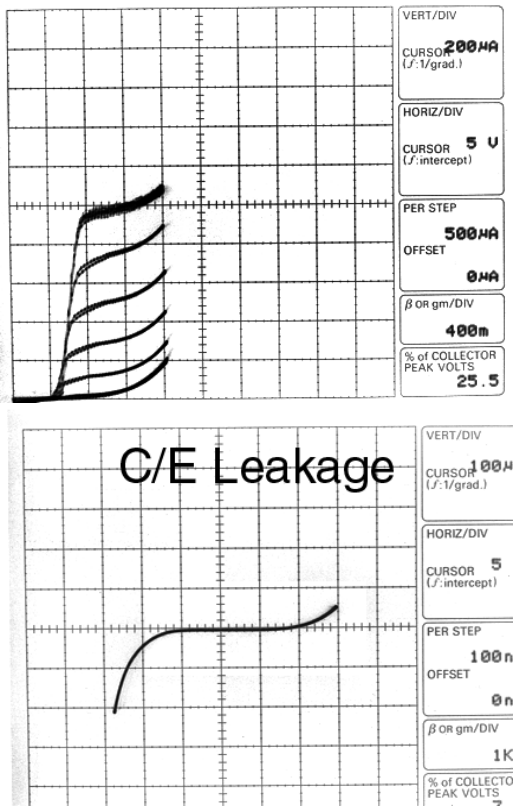

Figure 5.2:
Above: Common emitter characteristics of an MBE grown HBT showing high output conductance associated with large emitter-collector leakage.
Below: Collector emitter leakage measured directly for this device.

---

in Figure 5.3. Although the Gummel plot suggests a current gain of 50, the common emitter characteristic for the same device, Figure 5.4, shows that the actual current gain is less than unity. Common base characteristics as reported by some groups[5, 6], may also be misleading. This is because a collector-emitter leakage path will pass current without loss to the collector, and this may be misinterpreted as unity injection efficiency and transport. If the measurement is intended to demonstrate the transconductance of the device, care must be taken to drive the device with a voltage source rather than a current source. Transconductance is defined as $G_m = \partial I_C / \partial V_{BE}$. The parallel leakage path in the common base mode of the transistor may not be apparent when driven by a low output conductance current source, as the lower conductance of the source dominates.

Gummel plot of an HBT with high collector-emitter leakage

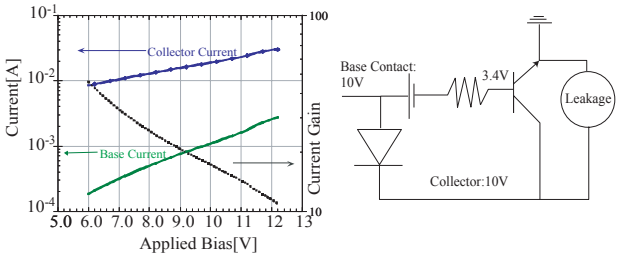

Figure 5.3: Gummel plot of a bipolar transistor with emitter collector leakage. The current gain seems high, as the collector current is much greater than the base current. From the circuit diagram, however, we see an example bias condition where the collector-emitter voltage is large, even when V_{BC}=0. Figure 5.4 shows the common emitter characteristic for this device.

Common emitter characteristics of an HBT with high collector-emitter leakage

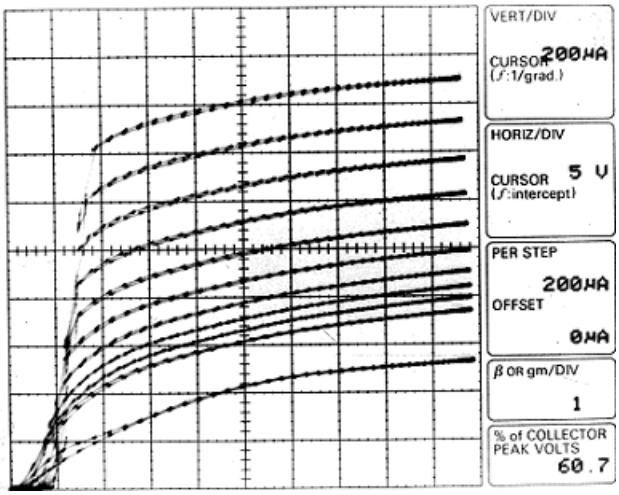

Figure 5.4: Common emitter characteristics corresponding to Gummel plot in Figure 5.3 Current gain is actually much lower than predicted by the Gummel plot.

5.3 Effects of dislocation density: HBTs on LEO GaN

To understand the source of the emitter-collector leakage in these devices, the connection between dislocation density and leakage current was investigated. Device structures were grown by MBE on MOCVD grown LEO templates. Transistors were

SEM micrograph of LEO Cross-section

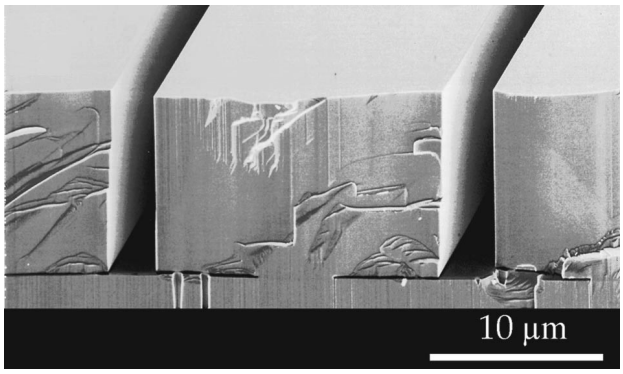

Figure 5.5: The above cross section shows an as-cleaved cross section of uncoalesced LEO stripes similar to those in the LEO template utilized for the AlGaN/GaN HBT on LEO GaN (courtesy P. Fini [9]).

fabricated on both the window region having relatively high dislocation densities (1×10^{8} cm^{-2}) and on the wing regions (having reduced dislocation densities $< 1\times10^{6}$ cm^{-2}).

5.3.1 Fabrication of HBTs on LEO GaN templates

The template or "Seed" growth process and active layer growth were as described in Chapter 2, and LEO growth is described below as discussed by P. Fini et al.[7]

> The LEO GaN stripes were grown on 2-μm-thick GaN "seed" [template] layers on 2 in. diam c-plane sapphire wafers. Plasma-enhanced chemical vapor deposition was used to deposit ∼200 nm of SiO_2, after which standard UV photolithographic patterning and wet chemical etching was used to define 5- μm-wide stripe openings in the SiO2. These stripes, oriented in the $\langle 1\bar{1}00\rangle$ GaN direction, were separated by 15 μmof SiO2, yielding a fill factor of 0.25. The LEO growth was performed in a vertical close-spaced reactor with a H2 carrier at an approximate surface temperature of 1060 °C, a reactor pressure of 76 Torr, and TMG and NH3 flows of 60 mmol/min and 0.885 slpm, respectively.
>
> — *From Fini et al. [7]*

Figure 5.5 shows an SEM micrograph of a representative LEO template film. Dislocation densities on LEO templates grown in the same lab have been reduced from $\sim 4\times10^{8}$ cm^{-2} to below 5×10^{6} cm^{-2}[8].

Diagram and AFM image of LEO grown template

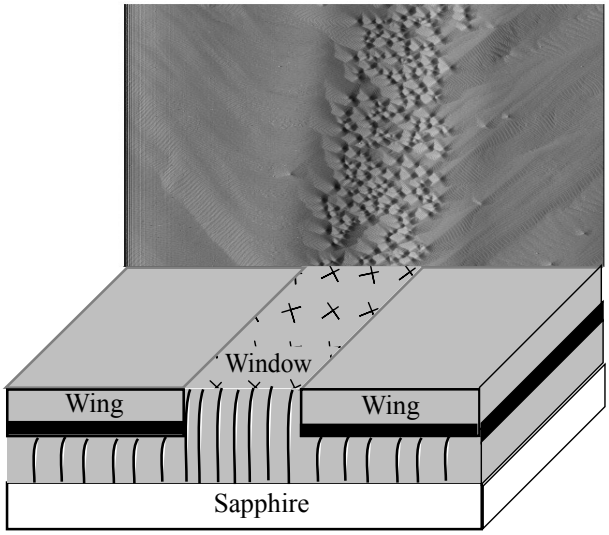

Figure 5.6: Atomic Force Microscopy image of an LEO substrate (above) showing window and ring regions. Spiral growth mode in the window region is associated with the screw component of TDs. Wing regions consist of atomically flat steps.

Active structure and device fabrication

After LEO template growth, a subcollector/collector structure was grown by MOCVD, followed by an active device structure by MBE. Figure 5.6 shows an AFM image and a diagram of the LEO template with MBE active layers grown on top. The features in the center of the AFM scan are representative of the spiral MBE growth morphology and indicative of TDs with screw character [10]. The smooth surface outside the window region illustrates the reduction in threading dislocations.

Devices were placed both entirely on the wing region, and entirely on the window region to determine the effect of dislocations on device performance. The devices tested had emitter mesa areas of 6μm x 50μm. Processing for the devices on LEO was the same as for the standard process.

5.3.2 Device results on LEO GaN

The collector-emitter leakage of adjacent devices was tested (Figure 5.7) and was seen to drop by four orders of magnitude in the forward direction on the wing relative to the window. Common-emitter characteristics of an HBT on a wing region are shown in Figure 5.8. The gain of the wing device is comparable to devices in the window (dislocated) regions. This result suggests that although dislocations are the dominating cause of collector-emitter leakage in these devices, at the present levels (10^{8} cm^{-2}) they are not the cause of the high recombination

Comparison of collector-emitter leakage on wing vs window

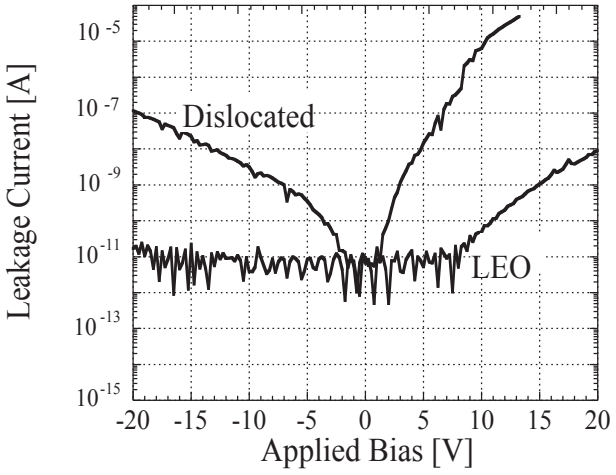

Figure 5.7: Semi log plot of leakage current of LEO window compared to wing region. Plot shows reduction of leakage by four orders of magnitude for wing region as compared to window region. The emitter mesa area for these devices was 6 μmx 50 μm.

Common emitter characteristics of an HBT on LEO GaN

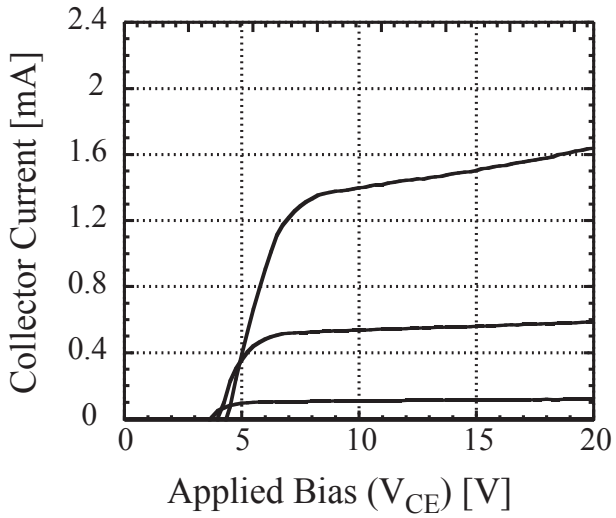

Figure 5.8: Common emitter characteristics of GaN HBT on LEO wing (non-dislocated region). Base current steps are 400μA.

rates in the base- which are expected to be related to the high Mg concentration (10^{20}cm^{-3}) and high levels of point defects.

5.4 Leakage vs. base doping

Although the dependence of the emitter collector leakage on dislocation density could be confirmed by fabricating devices on LEO templates, the mechanism was still not clear from the results. Experiments were performed to test the effect of base doping on emitter-collector leakage. An experiment was performed in which two devices were fabricated, both with lightly doped bases ($N_A = 10^{19} \Rightarrow p = 10^{17}$ cm^{-3}) 100 nm thick, on areas of the same template with the approximately the same TD density (5×10^8 cm^{-2} as estimated from pit density observed in an AFM scan). One of samples was grown with a 15 nm p^+ ($N_A = 10^{20} \Rightarrow p = 10^{18}$ cm^{-3}) spike in the center of the base to block emitter/collector leakage. The results of this experiment (Figure 5.9) show that the heavily doped spike in the neutral region of the base eliminated the emitter-collector short, suggesting that the mechanism for emitter-collector leakage may be the local compensation of the base layer.

5.5 Proposed emitter-collector leakage mechanism

The literature predicts that in n-type material, TDs behave as electron traps, and are negatively charged when filled. In p-type material, the TDs are expected to behave as donors, or hole traps, and thus be positively charged[11]. Various energy levels have been predicted for midgap states associated with TDs ranging from 0.6 eV to 3.2 eV above the valence band[12]. Because the leakage was found to be dependent on both dislocation density and base doping, a hypothesis was developed for the mechanism of this leakage using the following model: We assume that each TD contributes a line of charge in p-type GaN equivalent to one donor for every 10Å vertically, or 10^7 cm^{-1}. This was simulated as a column doped n-type at 3×10^{20} cm^{-3} and having a radius of 1 nm. The donor level is taken to be 3 eV above the valence band edge. This level is chosen because it is consistent with a low-voltage punch through observed at lower doping levels, as well as the energetically favorable dislocation configuration in both Ga rich and N rich growth conditions[12]. Figure 5.9 shows the effect of the local compensation on the p-type base. The result of this compensation in extreme cases - $N_A = 10^{19}$ cm^{-3} is a device that is shorted from collector to emitter. When the base doping concentration is sufficiently high - $N_A = 10^{20}$ cm^{-3}, however, a barrier remains to prevent the short. Although in this case the dislocations were found to be the dominant source of emitter-collector leakage, it should be noted that other mechanisms including surface states, mesa sidewall damage, and hop-

Effect of doping on emitter-collector leakage

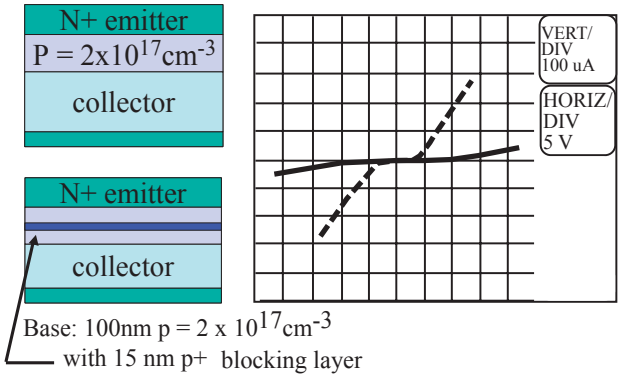

Figure 5.9: Emitter-Collector leakage is reduced by the addition of a p+ spike in the neutral base of a transistor structure. The solid line represents the emitter-collector leakage of the device with the p^+ blocking layer, while the dashed line is corresponds to the device with a conventional base doped p=2×10^{17} cm^{-3}.

ping conduction in the base may lead to emitter-base and base-collector leakage currents in addition to the dislocation induced leakage paths.

5.6 Summary

In summary, it was observed that many devices showed large emitter-collector leakage currents which led to high output conductance in some cases and unusable devices in others. Experiments were conducted on LEO templates with regions of reduced dislocation densities showing a correlation between threading dislocation density and emitter collector leakage. Although the devices fabricated on reduced dislocation regions showed several orders of magnitude reduction in leakage, the current gain of the devices was unchanged, suggesting that for these structures, dislocations were not responsible for the limited current gain. The mechanism responsible for this leakage was more apparent with the fabrication of devices with a layer of heavy base doping. The increased base doping reduced the collector-emitter leakage, suggesting a localized base punch-through effect around threading dislocations which are thought to act as a line of donor charge in the base layer. Band simulations confirm the plausibility of this explanation, showing the compensatory effect of a line of charge in the base layer. Although the devices showed significant improvement on LEO templates, due to the restrictions on geometry and added difficulty in fabrication and processing, future devices were not grown on LEO templates. Instead, subsequent to this study, only MOCVD templates with relatively low dislocation densities were used.

3D Illustration of a band diagram with a dislocation

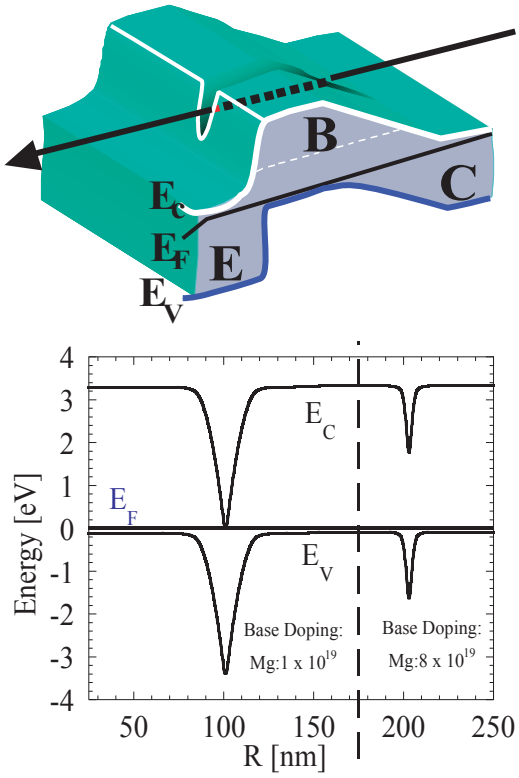

Figure 5.10:
Above: Three dimensional rendering of the proposed band diagram of an HBT with a dislocation (arrow) causing local compensation of the p-type base.
Below: Calculated cross sectional band-diagram of a locally compensated area surrounding a dislocation in p-type GaN taken at the base-emitter interface. A lightly doped base (left) is fully compensated near the dislocation, while a heavily doped base (right) is only partially compensated. The notches in the cross sectional band diagram correspond to the notch around the dislocation in the three dimensional illustration.

References

[1] Ren Fan, C. R. Abernathy, J. M. Van Hove, P. P. Chow, R. Hickman, J. J. Klaasen, R. F. Kopf, Cho Hyun, K. B. Jung, J. R. La Roche, G. Wilson, J. Han, R. J. Shul, A. G. Baca, and S. J. Pearton. 300 degrees c gan/algan heterojunction bipolar transistor. *MRS Internet Journal of Nitride Semiconductor Research*, 3, 1998.

[2] P. Kozodoy, J. P. Ibbetson, H. Marchand, P. T. Fini, S. Keller, J. S. Speck, S. P. DenBaars, and U. K. Mishra. Electrical characterization of gan p-n junctions with and without threading dislocations. *Applied Physics Letters*, 73(7):975–7, 1998.

[3] S. Nakamura. Role of dislocations in ingan-based leds and

laser diodes. pages 271–9, 2000.

[4] G. Parish, S. Keller, P. Kozodoy, J. P. Ibbetson, H. Marchand, P. T. Fini, S. B. Fleischer, S. P. DenBaars, U. K. Mishra, and E. J. Tarsa. Low dark current p-i-n (al,ga)n-based solar-blind uv detectors on laterally epitaxially overgrown gan. pages 175–8, 1999.

[5] X. A. Cao, G. T. Dang, A. P. Zhang, F. Ren, J. M. Van Hove, J. J. Klaassen, C. J. Polley, A. M. Wowchak, P. P. Chow, D. J. King, C. R. Abernathy, and S. J. Pearton. High current, common-base gan/algan heterojunction bipolar transistors. *Electrochemical and Solid-State Letters*, 3(3):144–6, 2000.

[6] Ren Fan, C. R. Abernathy, J. M. Van Hove, P. P. Chow, R. Hickman, J. J. Klaasen, R. F. Kopf, Cho Hyun, K. B. Jung, J. R. La Roche, G. Wilson, J. Han, R. J. Shul, A. G. Baca, and S. J. Pearton. 300 degrees c gan/algan heterojunction bipolar transistor. *MRS Internet Journal of Nitride Semiconductor Research*, 3, 1998.

[7] P. Fini, L. Zhao, B. Moran, M. Hansen, H. Marchand, J. P. Ibbetson, S. P. DenBaars, U. K. Mishra, and J. S. Speck. High-quality coalescence of laterally overgrown gan stripes on gan/sapphire seed layers. *Appl. Phys. Lett. (USA)*, 75(12):1706–8, 1999.

[8] H. Marchand, X. H. Wu, J. P. Ibbetson, P. T. Fini, P. Kozodoy, S. Keller, J. S. Speck, S. P. DenBaars, and U. K. Mishra. Microstructure of gan laterally overgrown by metalorganic chemical vapor deposition. *Applied Physics Letters*, 73(6):747–9, 1998.

[9] Paul T. Fini. *Threading dislocation reduction in gallium nitride thin films on sapphire via lateral epitaxial overgrowth*. PhD thesis, University of California, Santa Barbara, 2001.

[10] B. Heying, E. J. Tarsa, C. R. Elsass, P. Fini, S. P. DenBaars, and J. S. Speck. Dislocation mediated surface morphology of gan. *J. Appl. Phys. (USA)*, 85(9):6470–6, 1999.

[11] K. Leung, A. F. Wright, and E. B. Stechel. Charge accumulation at a threading edge dislocation in gallium nitride. *Appl. Phys. Lett. (USA)*, 74(17):2495–7, 1999.

[12] Lee Seung Mi, M. A. Belkhir, Zhu Xiao Yan, Lee Young Hee, Hwang Yong Gyoo, and T. Frauenheim. Electronic structures of gan edge dislocations. *Phys. Rev. B, Condens. Matter (USA)*, 61(23):16033–9, 2000.

6

Small Signal RF performance of the AlGaN/GaN HBT

6.1 Introduction

THE primary motivation behind the research into the AlGaN/GaN HBT was to investigate its potential as a high frequency power transistor, and to identify the major obstacles to that end. Although many barriers exist to the development of a GaN based HBT, the potential is clear from the basic material characteristics and past results both of HBTs in other material systems, and HEMTs in the AlGaN/GaN material system. AlGaN/GaN HEMTs, for example, have been produced with output current densities as high as 9.8 W/mm on SiC at 8GHz[1].

The fundamental material properties described in Table 6.1 can be used to predict potential RF performance of these devices and a comparison with a mature material system is helpful in assessing the potential of the GaN HBT. Lee et al. demonstrated AlInAs/GaInAs HBTs using a transferred substrate Schottky collector technology with a power gain cut-off frequency, f_{max}, of 820 GHz [2]. If this technology were applied to a GaN bipolar structure with a 50 nm base, having a carrier concentration of 5×10^{19} cm^{-3}, and a 100 nm thick collector, the predicted f_{max} is 200 GHz with a current gain cut-off frequency, f_t, of 200 GHz, and a 15V breakdown voltage. For power switching applications, material properties suggest that a 1 kV device with a collector thickness of 7μm, and a base thickness of 200 nm would have an f_t of 6 GHz and an f_{max} over 300 GHz.

Table 6.1: Comparison of material properties relevant to RF performance

Property	*GaN*	*GaInP*	*Si*
v_{sat} [cm/s]	20×10^6	10×10^6	6×10^6
E_{crit} [MV/cm]	2	0.6	0.3

In §6.2, the fabrication issues associated with producing devices that can be probed by standard CPW on wafer probes is discussed, with the DC characteristics presented in §6.3.1. Next, in §6.3.2, results of S-parameter measurements are used to determine the short circuit current gain cutoff frequency (f_t) and the maximum frequency of oscillation, f_{max}. The f_t of the device shows the unexpected behavior of a roll-off in current gain of -10 dB / decade with frequency. This is explained in §6.3.3, and simulations were performed to verify the plausibility of the explanation (§6.3.4).

Process flow for RF testable device

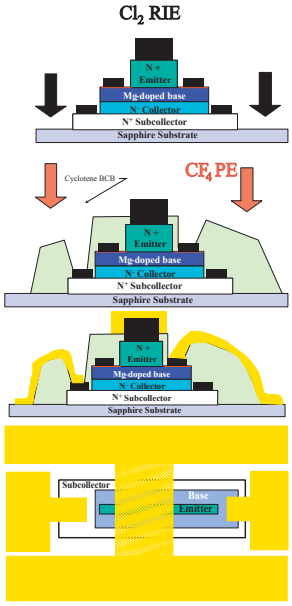

Figure 6.1: The process flow for fabricating CPW testing pads for GaN HBTs. First, a Cl_2 RIE etch isolates devices, then a thick layer of Cyclotene BCB is deposited to planarize the structure. A CF_4 plasma etch is used to etch back the BCB, exposing the emitter, and in a subsequent masked etch, openings are made for deposition of interconnect metals for the base and collector contacts. Finally, thick Ti/Au contact pads and interconnect metal are evaporated.

6.2 Device fabrication

The basic GaN HBT as described in Chapter 2 lacks the CPW pad structure necessary to test devices at high frequencies. As shown in Figure 6.1, the common emitter CPW pad layout requires an emitter or source pad on either side of the device with the base and collector pads at the ends. Also, to be compatible with the on-wafer CPW probes, the contact pads had to be much larger than was required for DC testing. After devices were fabricated for DC characterization, they could be further processed for RF testing.

First, a long Cl_2 RIE etch was used to isolate the devices to the sapphire substrate, and a layer of Cyclotene BCB spun on 15 μm

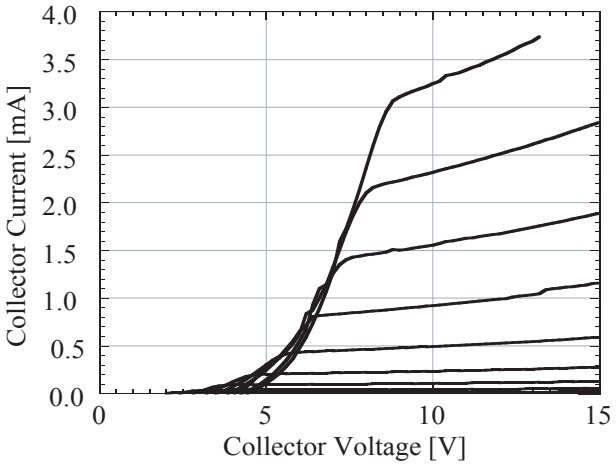

Figure 6.2: Common Emitter characteristics of the 3x50 μmdevice. Base current is in steps of 250 μA.

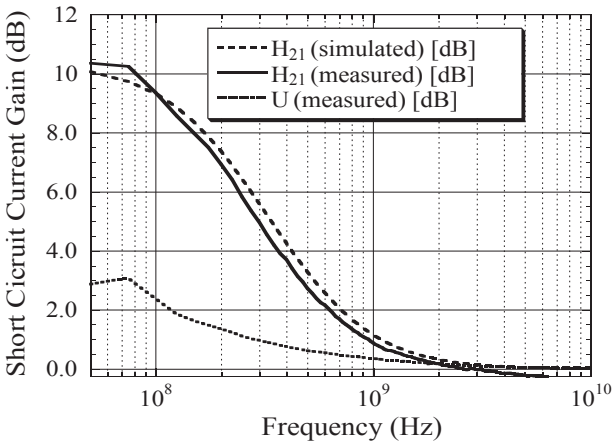

Figure 6.3: Small signal short circuit current gain (H_{21}) and Mason's unilateral gain (U) of device. I_C=4 mA. Simulated curve is a small signal simulation of the equivalent circuit shown in Figure 6.4

thick was used to planarize device structures. A blanket CF_4+O_2 plasma etch was used to etch back the BCB and expose the emitter contact. Openings were then etched in the BCB, exposing the base and collector contacts, and Ti/Au posts deposited. Contact pads and interconnect metal was then deposited and patterned using evaporation and lift-off.

6.3 Electrical characterization

6.3.1 DC device characterization

Before CPW pads were fabricated on these devices, DC testing was performed. The DC current gain was found to be 3.5 in common emitter mode (Figure 6.2). The higher than usual output conductance observed is likely due to leakage associated with threading dislocations. Although the DC current gain remained low, it was believed that a current gain of 3 was sufficient to show the basic small signal performance of the devices. The offset voltage was high, greater than 5 V, a result poor base contacts and the fact that this device was not fabricated with a regrown extrinsic base (See § 3.4.2). The device tested had an emitter area of 3×50 μmThe maximum emitter current density tested was over 3 kA cm^{-2} (assuming even spread across the emitter). In actuality, as explained in § 4.3.6, the active emitter width was probably much less than the actual width, resulting in an effective current density much greater than 3 $kAcm^{-2}$. Calculations using Eq 4.3.9 from Chapter 4 suggest a current density neglecting lateral spread which may be above 100 kA cm^{-2}, a value which is close to the onset of the Kirk effect.

6.3.2 RF device characterization

Small signal RF characterization with an Agilent Vector Network Analyzer (VNA) from 50MHz to 10GHz showed agreement with DC gain measurements at 50MHz, with a 3dB reduction in the short circuit current gain (H_{21}) at 200 MHz and a roll off of approximately 10dB/decade. The current gain cutoff frequency was 2 GHz, although the response with frequency became nearly flat after 1 GHz (See Figure 6.3).

Ideally, the current gain was expected to roll off with frequency at -20 dB/decade. This corresponds to a response from a single dominant pole. Because the roll-off of -10 dB/decade cannot be explained with a simple circuit model, a more complex mechanism seemed likely.

6.3.3 Distributed device model for RF performance

The non-ideal behavior of the device was thought to be due to the high sheet resistance of the base layer as well as high base contact resistances. The high resistance in the base leads to an equivalent circuit consisting of a distributed parasitic base-collector RC network which cannot be treated as a single RC time constant. Figure 6.4 shows a schematic of the proposed equivalent circuit with the parasitic resistances and capacitances included. The transistor is divided into three major blocks. The first, the extrinsic base, includes the majority of the base contact and the base-collector capacitance. Because the only resistance

Schematic of simulated equivalent circuit

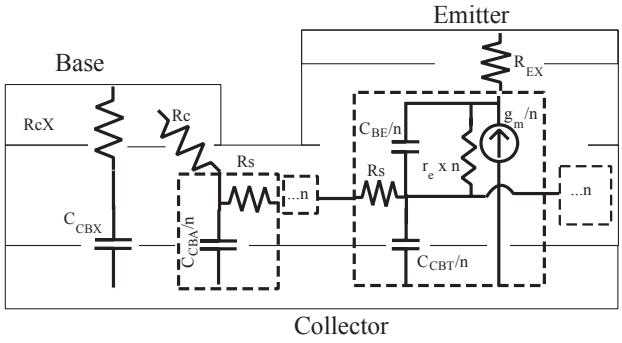

Figure 6.4: Schematic of equivalent circuit of simulated circuit drawn on cross sectional diagram of device structure. Dashed boxes represent repeated blocks. Each block is repeated 'n=25' times. The element values used in the simulation were as follows: C_{CBX} = 0.4 pF, RcX =60 Ω. C_{CBA} = 50 fF, C_{BE} = 0.6 pF, C_{CBT} = 30 fF, R_S = 100 kΩ/square, g_m=I_E/V_T = 350 mS, re = 3 Ω.

Simulated device geometry for RF device

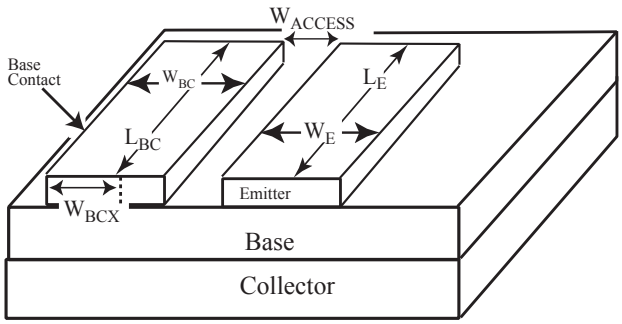

Figure 6.5: Diagram of the device geometry for the AlGaN/GaN HBT and the geometry used to model the small signal RF response of the device. Device dimensions are as follows (in microns): W_E =3, L_E = 50 , W_{Access} = 1, W_{BC} = 9, W_{BCX} = 8, L_{BC} = 72.

in this block is the vertical base contact resistance and series bulk resistances, this block can be treated as a lumped element. The second block is a repeated element including a series access base resistance and base-collector capacitance element. Finally, the active block consists of the familiar components of a simplified hybrid-Pi equivalent circuit model. This element includes a gain component as well as parasitic capacitances in the base-collector and base-emitter junctions. This element is repeated as well, separated by the bulk base access resistance. Each of these elements has a slightly different associated time constants, and the result is a continuum of time constants which together may lead to a reduction of H_{21} of ≈ 10 dB/decade in frequency as opposed to the usual 20 dB/decade.

6.3.4 Simulation of the RF distributed device

To confirm the plausibility of this model, a finite element small signal equivalent circuit simulation was carried out using HP ADS. The equivalent circuit shown in Figure 6.4 was simulated and the result plotted in Figure 6.3. A diagram of the relevant geometries of the device are shown in Figure 6.5.

To model the distributed nature of the device, the active and access blocks are repeated 25 times (indicated as 'n' in Figure 6.4). C_{CBX} = 0.4 pF represents the capacitance under the extrinsic base contact, and is in series with a vertical contact resistance, RcX = 60 Ω. C_{BC} also has a component in the access region to the base (C_{CBA} = 50 fF). Active device blocks contain a hybrid-pi small signal equivalent circuit element with a base-emitter capacitance (C_{BE} = 0.6 pF) and a base-collector capacitance element (C_{CBT} = 30 fF). The access and active blocks are connected by a sheet resistance, R_S = 100 kΩ/square. The small signal transconductance, g_m used was I_E/V_T = 350 mS, where V_T is the thermal voltage, 26 mV, and the emitter current, I_E was 9 mA. The values used in the simulation represent a measured R_s in the base, I_E, and approximate (within 5%) lumped capacitance values calculated from the geometry of the device. There were several adjustable parameters due to the difficulty in measuring a non-linear base contact resistance, R_{CX}, R_C, as well as an unknown emitter resistance, R_{EX} and unknown forward transit time (τ_F), where:

$$C_{BE} = C_{BE\ \text{Diffusion}} + C_{BE\ \text{Depletion}} \quad (6.3.1)$$

$$C_{BE\ \text{Diffusion}} = \tau_F \cdot g_m \quad (6.3.2)$$

Due to the many adjustable parameters, it is difficult to assert the correlation between all the values chosen for the simulation and actual device parasitics. It can be concluded, however, that the distributed finite element model gives a plausible explanation for the response of the device.

6.4 Summary

AlGaN/GaN HBTs with CPW probe pads were fabricated using a planarize and etch-back process with evaporated interconnects and contact pads. DC testing showed a typical current gain of ∼3.5. Although relatively low, this current gain was sufficient for preliminary investigations of the small signal RF behavior of these devices. S-parameter measurements showed a short-circuit current gain roll-off of -10 dB / decade, which was lower than the ideal 20 dB / decade. To explain this behavior, a distributed equivalent circuit was proposed which resulted in a continuum of time constants - potentially resulting in a roll off of

-10 dB/decade as observed. Because there were many adjustable parameters related to unknown material or device characteristics, however, a quantitative assessment of the major parasitic elements was not possible. Finite element simulations performed on this equivalent circuit showed the plausibility of this explanation and suggest a solution of reducing the bulk base resistance of the device to attain performance more closely matching the ideal response.

References

[1] Wu Yi-Feng, D. Kapolnek, J. P. Ibbetson, P. Parikh, B. P. Keller, and U. K. Mishra. Very-high power density algan/gan hemts. *IEEE Transactions on Electron Devices*, 48(3):586–90, 2001.

[2] Q. Lee, S. C. Martin, D. Mensa, R. P. Smith, J. Guthrie, S. Jaganathan, T. Mathew, S. Krishnan, S. Creran, and M. J. W. Rodwell. Submicron transferred-substrate heterojunction bipolar transistors with greater than 8000 ghz f/sub max. pages 175–8, 1999.

7

Conclusions and future work for the AlGaN/GaN HBT

CALCULATIONS based on the material properties of GaN show the
great potential of the HBT. Much of this dissertation has been focused on the investigation of the technological barriers to the realization of this potential. Although the difficulties in the growth and processing of GaN HBTs are significant, progress has been made toward identifying the dominant issues and working towards solutions. Limiting the performance of these devices , the p-type base suffers from low bulk conductivity, difficulty in processing, and low minority carrier lifetimes.

7.1 Parasitic offset voltage

In Chapter 3 it became clear that the damaging emitter mesa etch contributes to the extrinsic base resistance, affecting the offset voltage and reducing efficiency. Initial results suggest that although the parasitic offset voltage is significant, it can be effectively reduced by improving etch conditions and base layer conductivity. A more aggressive approach, the selectively regrown extrinsic base, also reduces the common emitter offset voltage, but requires more difficult processing which results in lower yields and repeatability.

7.1.1 Improving the offset voltage

Another approach to reducing the resistance associated with the base-emitter etch is the selectively regrown emitter HBT. Although this process was developed concurrently with the regrown extrinsic base HBT, it was not implemented until later by J. Limb et al. [1] and H. Xing et al.[2]. For this process, the base-collector structure is first grown by MOCVD or MBE, and then the base region is masked using sputtered AlN_x which provides a selective area regrowth mask for AlGaN layers. The emitter is selectively regrown by MOCVD, and conventional etch and lift-off techniques are used access the collector and to contact the base and emitter layers. In addition to reducing the offset voltage, these devices have shown increased current gains as well[2].

7.2 Current gain findings

Chapter 4 discussed the current gain of the AlGaN/GaN HBT, and various experiments were performed in an attempt to increase the current gain of the devices. It was concluded that due to the large effect of bandgap on injection efficiency that the emitter injection efficiency of the HBTs was near unity. A comparison of an HBT and BJT showed that assuming ideal injection in the HBT, and similar recombination rates throughout, the BJT injection efficiency can be calculated to be $\sim$90%. The low gains suggest, however, that recombination in the neutral base and in the space charge region of the base-emitter junction were limiting factors for these devices. Simulations suggested an improvement in current gain with a narrowing base and using base compositional grading to induce quasi-electric fields. Results showed some increase in gain, but perhaps due to the contributing emitter current crowding effects, the current gain remained limited.

7.2.1 Increasing current gain

To improve current gains, it is likely that material quality improvement in the base is required. Limitations on base doping prevent substantial narrowing of the base. Reducing the emitter current crowding effect may help, however, suggesting that narrower devices may have better results. Also, damaged sidewall and base surfaces may be recombination sites both in the space-charge region of the base-emitter junction and in the neutral base. It is likely that as in other material systems, the passivation of etched sidewalls will result in device performance improvement. Because emitter current crowding may be a contributing factor in sidewall and space charge region recombination, improvement of the base conductivity may also lead to higher current gains. Various methods have been proposed for the increase in lateral conductivity of base layers. Kozodoy et al. demonstrated an increase in lateral conductivity of p-type layers using an AlGaN/GaN superlattice[3]. Unfortunately this results in conduction band barriers that are likely to increase the base transit time of electrons.

7.3 The effect of dislocations on AlGaN / GaN HBT characteristics

The effect of dislocations on the device characteristics of the HBT were presented in Chapter 5. As expected from previous studies[4], the vertical leakage is related strongly to dislocation density. For the HBT, however, this leakage can result in misleading electrical measurements. Gummel plots and common base characteristics of HBTs with significant collector-emitter leakage may confuse leakage with transport efficiency. The fabrication of devices on LEO substrates demonstrated the effect of dislocations on leakage, and experiments studying the effect of

base doping on leakage on dislocated substrates suggested that the leakage mechanism was a localized punch-through effect.

7.3.1 Reducing the effect of dislocations

Although it is possible to fabricate devices with low output conductance by choosing substrates with relatively low dislocation densities, more work is needed to understand possible secondary effects of the dislocations on characteristics such as current gain, reliability, and breakdown. Although the long term prospects of HBTs fabricated on LEO substrates is questionable due to the current dimensional limitations and difficulty in processing associated with this technique, there is motivation here and in other devices for the reduction of threading dislocation densities. Thicker layers, GaN substrates, and self-masking coalesced templates are all possibilities.

7.4 RF performance

The small signal S-parameters of the AlGaN/GaN HBT were presented in Chapter 6. The most notable result was the non-ideal behavior of the short-circuit current gain (H_{21}) of the devices. The current gain dropped at -10dB/decade as opposed to the ideally predicted -20dB/decade. Analysis suggested that this was due to the low conductivity of the base layer. Finite element device simulations confirm that the high base resistance may cause a distributed device effect, resulting in a continuum of time constants that result in a reduced roll-off rate similar to measured results. It is clear that the power gain for the device will continue to be limited as long as the base resistance remains high. Although only small signal characteristics for the device were measured, the requirements of a power amplifier may be the most demanding on the conductivity of the base layer.

7.4.1 Improving RF performance

In addition to increasing the base conductivity for the npn HBT, another opportunity exists in the fabrication of the AlGaN/GaN or GaN/InGaN/GaN p-n-p HBTs. Although a process for this was developed, and fabrication attempted, these efforts were unsuccessful at UCSB over the course of this dissertation. The advantages of the p-n-p transistor lay primarily in the enhanced conductivity of the n-type base. Because the n-type dopant is shallow, much greater carrier densities can be attained at similar dopant levels. The high mobility of electrons in n-layers also enhances base conductivity, and etch-damage during the emitter mesa etch ceases to be a problem. Unfortunately, the minority carrier diffusivity of holes in the highly doped n-type base, and their drift velocity in the collector is likely to be quite low due to the high effective mass of holes. Also, due to the deep acceptor in the emitter of the p-n-p, it is necessary to strongly dope the emitter to reduce emitter resistance. Unfortunately this may lead to a narrow depletion region and increased base-emitter parasitic capacitance.

7.5 Current status of AlGaN/GaN HBTs

This dissertation represents work in the first AlGaN/GaN HBTs to be fabricated. After the first few devices were fabricated, two approaches for the fabrication of the AlGaN/GaN HBT were identified – the etched emitter, and regrown emitter HBT. It was determined that for the etched emitter device, MBE growth was preferable, while for the selectively regrown device, MOCVD was the preferred growth technique. At the time, very little was known about the minority carrier mobility or lifetime in p-type GaN grown by MOCVD or MBE. More recently, reports suggest that MBE grown Mg doped films may suffer from faceted inversion domains [5], which if present in the AlGaN/GaN HBT may lead to reduced minority carrier lifetimes. Although the work with MBE grown devices represented by the bulk of this dissertation was important in understanding the key elements of device performance relevant the AlGaN/GaN HBT, it is necessary to point out that many of the limiting factors for the etched emitter MBE grown HBT may not be dominant in, for example, an MOCVD regrown emitter HBT. For instance, recent results using that technique have shown current gains over 20 in an AlGaN/GaN HBT with a similar structure [6], confirming the promise of the MOCVD regrown emitter device. In addition to the obvious advantage of increasing the current gain, the reduction in base current associated with higher gains reduces the emitter current crowding problem as well as many other "distributed device" effects associated with large voltage drops in the base. Also, Makimoto et al. reported GaN/InGaN/GaN DHBTs with current gains of 20 at room temperature. The base majority carrier concentration in this material was 5×10^{18}cm^{-3}with a Mg concentration of 1×10^{19}cm^{-3} (possibly due to a shallower acceptor ionization energy).

7.6 Summary

In summary, the material, growth, and processing issues associated with the Mg doped base layer have dominated the characteristics of the AlGaN/GaN HBT and therefore represent the greatest need for improvement for the progress of the HBT. Progress has been made, however in identifying the major issues in the DC and RF performance of the HBT. Devices have been fabricated on MOCVD and MBE active layers of varying structure including compositionally graded bases, and base layers of varying thickness and doping concentration. The cause of the parasitic offset voltage in the common emitter output characteristics has been investigated, and addressed in the extrinsic regrown base HBT as well as in process improvements associated with the emitter mesa etch and the base metalization process. The effects of dislocations were investigated by fabricating devices on LEO substrates and measuring the collector-emitter leakage as a function of dislocation density and base doping profile. The leakage mechanism was found to be a localized punch through effect surrounding the dislocation. Finally, a process was developed for fabricating CPW compatible devices, and devices were

tested and shown to have an f_t of 2GHz. The gain/frequency characteristic was un-ideal, however, and finite element simulations confirm that this may be due to the low conductivity in the base.

As improvements are made to the base conductivity and minority carrier lifetime, it is hoped that the AlGaN/GaN HBT will begin to approach its potential as a valuable high frequency, high power device. Currently, work continues, and improvements promise to overcome many of the barriers presented in this dissertation.

References

[1] J. B. Limb, L. McCarthy, P. Kozodoy, H. Xing, J. Ibbetson, Y. Smorchkova, S. P. DenBaars, and U. K. Mishra. Algan/gan hbts using regrown emitter. *Electronics Letters*, 35(19):1671–3, 1999.

[2] H. Xing, L. McCarthy, S. Keller, S. P. DenBaars, and U. K. Mishra. High current gain gan bipolar junction transistors with regrown emitters. pages 365–9, 2000.

[3] P. Kozodoy, Y. P. Smorchkova, M. Hansen, Xing Huili, S. P. DenBaars, and U. K. Mishra. Polarization-enhanced mg doping of algan/gan superlattices. *Applied Physics Letters*, 75(16):2444–6, 1999.

[4] P. Kozodoy, J. P. Ibbetson, H. Marchand, P. T. Fini, S. Keller, J. S. Speck, S. P. DenBaars, and U. K. Mishra. Electrical characterization of gan p-n junctions with and without threading dislocations. *Applied Physics Letters*, 73(7):975–7, 1998.

[5] L. T. Romano, J. E. Northrup, A. J. Ptak, and T. H. Myers. Faceted inversion domain boundary in gan films doped with mg. *Applied Physics Letters*, 77(16):2479–81, 2000.

[6] H. Xing, P. Chavarkar, S. Keller, S. DenBaars, and U. Mishra. Algan/gan heterojunction bipolar transistors with gain over 20 at room temperature. *To be submitted*.